



# Large strained fracture of nearly incompressible hyperelastic materials: Enhanced assumed strain methods and energy decomposition

Jia-Yu Ye<sup>a</sup>, Lu-Wen Zhang<sup>a,\*</sup>, J.N. Reddy<sup>b</sup>

<sup>a</sup> Department of Engineering Mechanics, School of Naval Architecture, Ocean and Civil Engineering, Shanghai Jiao Tong University, Shanghai 200240, China

<sup>b</sup> Advanced Computational Mechanics Lab, Department of Mechanical Engineering, Texas A&M University, College Station, TX 77843-3123, USA



## ARTICLE INFO

### Article history:

Received 3 February 2020

Revised 5 March 2020

Accepted 14 March 2020

Available online 19 March 2020

### Keywords:

Phase-field model

Hyperelasticity

Energy decomposition

Assumed strain method

Incompressible problem

## ABSTRACT

Tracking crack propagation at large strains of hyperelastic solids is a challenging task due to the high nonlinearity, nearly incompressibility and ordered tendency in microstructure of the rubbery material under stretch. On the basis of the diffusive crack model, this work presents a new phase-field model by combining the strain energy decomposition and the enhanced assumed strain method. The proposed fracture formulation is indeed Griffith's theory-based framework but further accounting for the coupled effects of the stretches, damage and incompressibility to predict the crack growth in both compressible and incompressible hyperelastic solids. There are three innovations contained in this study: (i) The developed phase-field framework is capable to capture the effect of hole collapse, which is an intrinsic phenomenon of hyperelastic material and difficult to be detected by the others. (ii) The developed energy decomposition method provides a reasonable description of the physical reality that the hyperelastic fracture is driven by the changes in the internal energy of the stretched molecular chains in the polymer network. This continuum description automatically distinguishes the strain energy that really contributes to crack growth at multiaxial stress states, reducing significantly the numerical instability caused by material softening. (iii) By introducing the assumed strain method to the present fracture scheme, the physical consistency of energy decomposition and the mathematical nonnegativeness of strain energy can be satisfied simultaneously for incompressible problem. We demonstrate the performance of the enhanced phase-field framework through representative examples and highlight the importance of positive deviatoric energy for incompressible problem by comparing with experiments and classical models.

© 2020 Elsevier Ltd. All rights reserved.

## 1. Introduction

Hyperelastic materials play an important role in both mature industrial productions and future-oriented applications, such as rubber sealer, elastomeric foam, hydrogen gels for flexible electronics and biomaterials, and others. Although the fracture modes of most hyperelastic materials belong to brittle fracture based on Griffith's configurational energy driven

\* Corresponding author.

E-mail address: [lwzhang@sjtu.edu.cn](mailto:lwzhang@sjtu.edu.cn) (L.-W. Zhang).

theory, their fracture process is accompanied by highly material and geometric nonlinearity. In applications where the hyperelastomers are not highly confined, most hyperelastic materials have very little compressibility compared to their shear flexibility, such as polybutadiene and styrene butadiene rubber, and it would be quite reasonable to presume that the material is nearly incompressible.

The incompressibility of elastomers is intrinsically determined by its microscopic network structure of polymer chains. Numerous microcosmic models are proposed to establish a link with the macro material properties and microstructural features, e.g. the tube model (Heinrich and Kaliske, 1997), the eight chains model (Boyce and Arruda, 2000), the non-affine micro-sphere model (Miehe et al., 2004). These micro-mechanically driven models, which is developed from consideration of free motions of a single chain to topological constraints around the junctions, shows an improved agreement with experimental results, but suffer in fitting a number of physically based materials coefficients. Macroscopic approximations of isotropic elastomers are formulated in terms of strain energy potential in different polynomial forms: the Ogden form (Ogden, 1997), the Marlow form, the Mooney-Rivlin form, the neo-Hookean form, Arruda-Boyce form et al. However, these well-established phenomenological models lack relations to the configuration of molecular chains and network structures. In order to balance efficiency and robustness to facilitate realistic applications, we advance the current study of modeling the fracture failure of hyperelastic materials to account the network structure of polymer chains within the framework of phenomenological continuum mechanics, which will be discussed in Section 3 in details.

Fracture failure and crack propagation has been investigated extensively by the discrete concept based numerical implementations of sharp crack discontinuity, e.g. element erosion methods (Pandolfi and Ortiz, 2012; Song et al., 2008), interelement separation methods (Ortiz and Pandolfi, 1999; Pandolfi et al., 2000), hybrid discrete FEM (Azevedo and Lemos, 2006), generalized FEM (Duarte et al., 2001), and extended FEM (Sukumar et al., 2000). These discrete fracture modeling methods require remeshing in the explicit treatment of the boundary conditions at the moving fracture surfaces, leading to high complexity in the interactive procedure when dealing with crack bifurcations and intersections, especially for three-dimensional fracture problems at large strains.

Compared to the discrete strategies, phase-field model is efficient in tracking crack path in a continuous manner (Choo and Sun, 2018; Sabnis et al., 2016) by following the basis of the Griffith fracture mechanics theory and its pioneering works (Bourdin et al., 2000; Francfort and Marigo, 1998). The phase-field formulation provides a regularized description of sharp crack topologies through a scalar continuous phase-field variable. Moreover, it can be applied to nearly all the fracture problems owing to its flexible multi-field framework, e.g. the interfacial fracture (Nguyen et al., 2016; Paggi and Reinoso, 2017), dynamic fracture (Borden et al., 2012; Geelen et al., 2019), hydraulic fracture (Miehe et al., 2015b; Wilson and Landis, 2016), and anisotropic fracture (Li and Maurini, 2019; Shanthraj et al., 2017).

Note that the large deformed fracture of elastomers is driven by the change in a part of strain energy rather than the total strain energy, thereby the strain energy in the phase-field model has to be decomposed to account the real contribution to the fracture. A novel energy decomposition method was proposed to distinguish the tensile and compressive effects on the crack growth by Miehe et al. (2010). This concept has been widely applied for the linear elastic materials (Gerasimov and De Lorenzis, 2016; Seles et al., 2019). As for nonlinear elastic problems, an extensive energy decomposition method that involves volumetric-deviatoric decomposition was proposed (Borden et al., 2016) and applied to ductile materials (Miehe et al., 2015a), viscoelastic materials (Shen et al., 2019), and hyperelastic materials (Wu et al., 2016).

However, the volumetric-deviatoric decomposition method is still hindered by the numerical instability rooted in the material nonlinearity, such as softening, which turns out to form a singular tangent stiffness matrix in the implicit integration scheme, resulting in nonconvergence and collapsibility in numerical analysis. To improve the stability of solution, Zhang et al. (2002) added damping and viscous terms to represent the dissipation of the released strain energy. Thiagarajan et al. (2004) applied an explicit time integration scheme to avoid inversion of the singular matrix in the implicit integration scheme, but at the expense of accuracy. Recently, Tang et al. (2019) proposed an energy decomposition method that distinguishes tensile and principal stretches in Neo-Hookean strain energy potential, efficiently reducing the numerical instability without losing accuracy.

Fracture in the constrained media problems has been well studied by the phase-field model in the recent works, such as the fracture in plates and shells with infinitesimal deformations (Areias et al., 2016a) and the solid within quasi-incompressible problem (Areias et al., 2016b). Moreover, for constrained media like incompressible hyperelastic materials, it is a challenge in incorporating both the energy decomposition and incompressibility into the phase-field model, because of the requirement on nonnegativeness of strain energy. The numerical iteration cannot be continued, unless the decomposed energies are nonnegative mathematically. There are very few papers in the literature which address the strain energy decomposition for incompressible materials. The only paper that we are aware of is the very recent work of Li and Bouklas (2020). They formulated a displacement-pressure mixed phase-field model to simulate the crack propagation in the incompressible polymer, however, did not adopt the strategy of energy decomposition, leaving the problem of numerical instability unsolved.

In the present study, the enhanced assumed strain (EAS) method is introduced into the phase-field model to resolve the contradiction (the nonnegativeness of strain energy) between energy decomposition and incompressibility. The EAS method was proposed (Simo and Armero, 1992; Simo and Rifai, 1990) for developing efficient elements, and reducing the volume deformation to meet the incompressibility constraint (Caseiro et al., 2015; Videla et al., 2019). Therefore, by incorporating this strategy with energy decomposition into the phase-field model, the proposed model can be readily used to describe the fracture at large strains of incompressible elastomers without losing the nonnegativeness of strain energy.

The remainder of this paper is organized as follows. The fundamentals of the assumed strain method and its Hu-Washizu three-field variational formulation are given in Section 2. In Section 3, the governing equations of the phase-field model are presented, following which the present energy decomposition method and the mathematical proof of the nonnegativeness with the incompressible problems are given. Subsequently, in Section 4, the variational formulation and multi-field finite element implementation are addressed. Section 5 provides numerical examples of compressible and incompressible hyperelastic materials, and the corresponding experimental characterizations are provided for discussion and analysis. The main conclusions are presented in Section 6.

## 2. Static modeling of compressible/incompressible hyperelastic materials

To illustrate the proposed multi-field framework, we show in this section the static response of the compressible isotropic solids by the displacement field. The Hu-Washizu three-field variational formulation is introduced to yield the Euler-Lagrange equations. Subsequently, the assumed strain field is embedded to formulate enhanced three-field variational for the incompressible problems.

### 2.1. The Hu-Washizu three-field variational formulation of compressible hyperelastic materials

Let  $\Omega_0 \subset \mathbb{R}^{SD}$  (with  $SD \in \{1, 2, 3\}$ ) be the reference configuration of an arbitrary body with the external boundary  $\partial\Omega_0 \subset \mathbb{R}^{SD-1}$ , and the closure  $\bar{\Omega}_0 := \Omega_0 \cup \partial\Omega_0$ . The deformation of the body from its reference configuration is described by the displacement field  $\mathbf{u} : \bar{\Omega}_0 \rightarrow \mathbb{R}^{SD}$ , with the displacement boundary condition  $\mathbf{u} = \bar{\mathbf{u}}$  on  $\Gamma_u \subset \partial\Omega_0$ . The nominal traction is prescribed as  $\bar{\mathbf{p}} : \Gamma_s \rightarrow \mathbb{R}^{SD}$  on the force boundary  $\Gamma_s \subset \partial\Omega_0$ , where

$$\partial\Omega_0 = \Gamma_u \cup \Gamma_s \text{ and } \Gamma_u \cap \Gamma_s = \emptyset. \quad (1)$$

The current configuration at time  $t$  and its external boundary are denoted as  $\Omega_t$  and  $\partial\Omega_t$ , respectively. The time dependent deformation  $\mathfrak{N} : (\Omega_0 \times \mathbb{R}) \rightarrow \Omega_t$  maps a point  $\mathbf{X} \in \Omega_0$  to another  $\mathbf{x} = \mathfrak{N}(\mathbf{X}, t) \in \Omega_t$  at time  $t \in [0, T]$ . The compatible deformation gradient is defined as

$$\mathbf{F} = \nabla \mathfrak{N}(\mathbf{X}, t) = \frac{\partial \mathfrak{N}(\mathbf{X}, t)}{\partial \mathbf{X}}. \quad (2)$$

We shall denote by  $\tilde{\Psi}$  the strain energy function, given as

$$\tilde{\Psi} = \tilde{\Psi}(\mathbf{X}, \mathbf{F}). \quad (3)$$

In order to imply the frame invariance, we define  $\mathbf{C} = \mathbf{F}^T \mathbf{F}$ , and then a modified strain energy function is given as

$$\tilde{\Psi}(\mathbf{X}, \mathbf{F}) = \tilde{\Psi}(\mathbf{X}, \mathbf{C}). \quad (4)$$

We further assume that the arbitrary body is subjected to external load and body force per unit of mass:  $\mathbf{b}_0 : \Omega_0 \rightarrow \mathbb{R}^{SD}$ . Then the external potential energy takes the form

$$\Pi_{ext}(\mathbf{u}) = - \int_{\Omega_0} \rho_0 \mathbf{b}_0 \cdot \mathbf{u} dV - \int_{\Gamma_t} \bar{\mathbf{T}} \cdot \mathbf{u} d\Gamma, \quad (5)$$

where  $\rho_0 : \Omega_0 \rightarrow \mathbb{R}^{SD}$  is the reference density and  $\bar{\mathbf{T}}$  is the prescribed nominal traction vector.

Now consider a formulation of nonlinear elasticity of the Hu-Washizu type in which the displacement field  $\mathbf{u}$ , the compatible displacement gradient  $\mathbf{H}$  and the nominal stress tensor  $\mathbf{P}$  are regarded as independent variables. The three-field functional  $\Pi$  is defined by

$$\Pi(\mathbf{u}, \mathbf{H}, \mathbf{P}) = \int_{\Omega_0} [\tilde{\Psi}(\mathbf{X}, \mathbf{C}) + \mathbf{P}(\nabla \mathbf{u} - \mathbf{H})] dV + \Pi_{ext}(\mathbf{u}). \quad (6)$$

The variation of  $\Pi(\mathbf{u}, \mathbf{H}, \mathbf{P})$  is then given as

$$\delta \Pi = \int_{\Omega_0} \left[ 2 \frac{\partial \tilde{\Psi}}{\partial \mathbf{C}} \mathbf{F}^T - \mathbf{P} \right] \delta \mathbf{H} + \delta \mathbf{P}(\nabla \mathbf{u} - \mathbf{H}) dV + \int_{\Omega_0} \mathbf{P} \delta(\nabla \mathbf{u}) dV + \Pi_{ext}(\delta \mathbf{u}). \quad (7)$$

Standard arguments in the calculus of variation Eq. (7) yields the local Euler-Lagrange equations as following

$$\begin{cases} \nabla \cdot \mathbf{P} + \rho_0 \mathbf{b}_0 = 0, \\ \nabla \mathbf{u} - \mathbf{H} = 0, \\ 2 \frac{\partial \tilde{\Psi}}{\partial \mathbf{C}} \mathbf{F}^T - \mathbf{P} = 0, \end{cases} \quad \forall \mathbf{X} \in \Omega_0, \quad (8)$$

with the boundary conditions

$$\mathbf{P} \cdot \mathbf{N} = \bar{\mathbf{T}} \text{ on } \Gamma_s, \quad (9)$$

where  $\mathbf{N}$  is the unit normal vector to the boundary  $\partial\Omega_0$ .

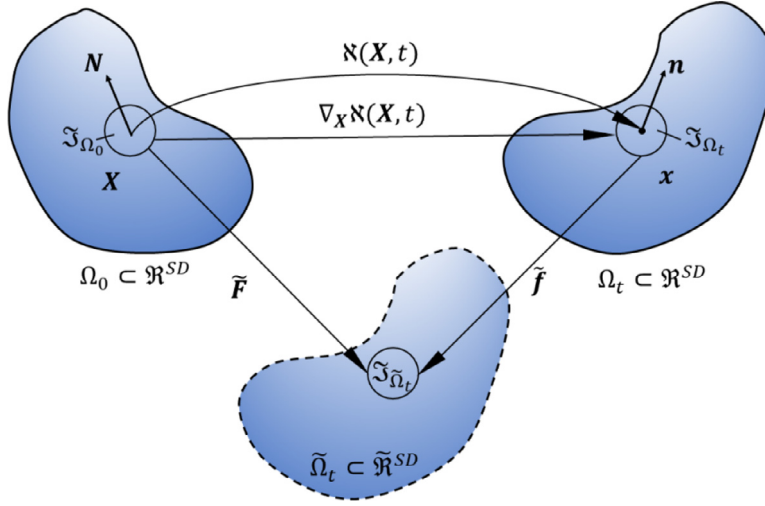


**Fig. 1.** The assumed deformation gradient  $\tilde{\mathbf{F}}$  represents two independent mappings: the compatible mapping, which maps  $\mathfrak{S}_{\Omega_0}$  to  $\mathfrak{S}_{\Omega_t}$  through  $\nabla_X \mathbf{N}$ ; The enhanced mapping which maps  $\mathfrak{S}_{\Omega_t}$  to  $\tilde{\mathfrak{S}}_{\Omega_t}$  through  $\tilde{\mathbf{f}}$ .  $\mathfrak{S}_{\Omega_0}$ ,  $\mathfrak{S}_{\Omega_t}$  and  $\tilde{\mathfrak{S}}_{\Omega_t}$  represent the local neighborhood in the reference configuration  $\Omega_0$ , the current configuration  $\Omega_t$  and the virtual configuration  $\tilde{\Omega}_t$ , respectively. The whole mapping process satisfies  $J = |\tilde{\mathbf{F}}| = |\tilde{\mathbf{f}} \nabla_X \mathbf{N}| = 1$ .

## 2.2. The enhanced three-field variational formulation of incompressible hyperelastic materials

Following [Simo and Armero \(1992\)](#), we represent the assumed displacement gradients  $\mathbf{H}$  in terms of the compatible displacement gradient  $\nabla \mathbf{u}$  and the enhanced displacement gradient  $\tilde{\mathbf{H}}$  as

$$\mathbf{H} = \nabla \mathbf{u} + \tilde{\mathbf{H}}. \quad (10)$$

The assumed deformation gradient  $\tilde{\mathbf{F}}$  is defined as a function of  $\mathbf{u}$  and  $\tilde{\mathbf{H}}$ :

$$\tilde{\mathbf{F}} = \mathbf{1} + \mathbf{H} = \mathbf{1} + \nabla \mathbf{u} + \tilde{\mathbf{H}}, \quad (11)$$

where  $\mathbf{1}$  is an  $N_{SD} \times N_{SD}$  identity matrix. Eq. (11) is in the form of additive decomposition that can be reformulated as an equivalent form of multiplicative decomposition:

$$\tilde{\mathbf{F}} = \mathbf{1} + \nabla \mathbf{u} + \tilde{\mathbf{H}} = (\mathbf{1} + \tilde{\mathbf{H}} \nabla^{-1} \mathbf{N}) \nabla_X \mathbf{N} = \tilde{\mathbf{f}} \nabla_X \mathbf{N}, \quad (12)$$

where  $\nabla_X \mathbf{N}$  is the compatible deformation gradient,  $\tilde{\mathbf{f}}$  is the enhanced deformation gradient, and  $\tilde{\mathbf{f}} = \mathbf{1} + \tilde{\mathbf{H}} \nabla^{-1} \mathbf{N}$ . A compatible relationship is established between the current configuration  $\Omega_t$  and the reference configuration  $\Omega_0$  through the compatible deformation gradient  $\nabla_X \mathbf{N}$ , as shown in Fig. 1. However,  $\nabla_X \mathbf{N}$  cannot be used to describe the incompressible deformation because the incompressibility constraint in the compatible mapping is not satisfied, i.e.  $J = |\nabla_X \mathbf{N}| \neq 1$ . This problem can be solved by incorporating an enhanced deformation gradient  $\tilde{\mathbf{f}}$ , thereafter a virtual configuration  $\tilde{\Omega}_t$  in the assumed strain space  $\tilde{\mathfrak{H}}^{SD}$  can be obtained by mapping the current configuration  $\Omega_t$  with the enhanced deformation gradient  $\tilde{\mathbf{f}}$ . Therefore, the incompressibility constraint  $J = |\tilde{\mathbf{F}}| = |\tilde{\mathbf{f}} \nabla_X \mathbf{N}| = 1$  can be satisfied perfectly in the virtual configuration  $\tilde{\Omega}_t$ .

Now let  $\tilde{\Pi}(\mathbf{u}, \tilde{\mathbf{H}}, \mathbf{P})$  be the enhanced Hu-Washizu function, which is defined by

$$\tilde{\Pi}(\mathbf{u}, \tilde{\mathbf{H}}, \mathbf{P}) = \int_{\Omega_0} [\tilde{\Psi}(\mathbf{X}, \tilde{\mathbf{C}}) + \mathbf{P}(\nabla \mathbf{u} - \mathbf{H})] dV + \Pi_{ext}(\mathbf{u}) = \int_{\Omega_0} [\tilde{\Psi}(\mathbf{X}, \tilde{\mathbf{C}}) - \mathbf{P} \tilde{\mathbf{H}}] dV + \Pi_{ext}(\mathbf{u}), \quad (13)$$

and its variation is given by

$$\begin{aligned} \delta \tilde{\Pi} &= \int_{\Omega_0} \left[ 2 \frac{\partial \tilde{\Psi}}{\partial \tilde{\mathbf{C}}} \tilde{\mathbf{F}}^T \delta(\nabla \mathbf{u}) + 2 \frac{\partial \tilde{\Psi}}{\partial \tilde{\mathbf{C}}} \tilde{\mathbf{F}}^T \delta \tilde{\mathbf{H}} - \tilde{\mathbf{H}} \delta \mathbf{P} - \mathbf{P} \delta \tilde{\mathbf{H}} \right] dV + \Pi_{ext}(\delta \mathbf{u}) \\ &= \int_{\Omega_0} \left[ - \left( \nabla \cdot 2 \frac{\partial \tilde{\Psi}}{\partial \tilde{\mathbf{C}}} \tilde{\mathbf{F}}^T + \rho_0 \mathbf{b}_0 \right) \delta \mathbf{u} + 2 \left( \frac{\partial \tilde{\Psi}}{\partial \tilde{\mathbf{C}}} \tilde{\mathbf{F}}^T - \mathbf{P} \right) \delta \tilde{\mathbf{H}} - \tilde{\mathbf{H}} \delta \mathbf{P} \right] dV + \int_{\Gamma_t} (2 \frac{\partial \tilde{\Psi}}{\partial \tilde{\mathbf{C}}} \tilde{\mathbf{F}}^T - \tilde{\mathbf{T}}) \delta \mathbf{u} d\Gamma, \end{aligned} \quad (14)$$

or equivalently

$$\begin{cases} \int_{\Omega_0} \left( 2 \frac{\partial \tilde{\Psi}}{\partial \tilde{\mathbf{C}}} \tilde{\mathbf{F}}^T \delta(\nabla \mathbf{u}) + \rho_0 \mathbf{b}_0 \delta \mathbf{u} \right) dV = 0, \\ \int_{\Omega_0} \left( 2 \frac{\partial \tilde{\Psi}}{\partial \tilde{\mathbf{C}}} \tilde{\mathbf{F}}^T - \mathbf{P} \right) \delta \tilde{\mathbf{H}} dV = 0, \\ \int_{\Omega_0} \delta \mathbf{P} \cdot \tilde{\mathbf{H}} dV = 0, \end{cases} \quad \forall \mathbf{X} \in \Omega_0, \quad (15)$$

where  $\tilde{\mathbf{C}} = \tilde{\mathbf{F}}^T \tilde{\mathbf{F}}$  is the assumed right Cauchy-Green tensor. According to the Eq. (15)<sub>2</sub>, we have  $2 \frac{\partial \tilde{\Psi}}{\partial \tilde{\mathbf{C}}} \tilde{\mathbf{F}}^T = \mathbf{P}$ , which can be substituted into the last term of Eq. (14), then the boundary conditions is given as

$$\mathbf{P} \cdot \mathbf{N} = \tilde{\mathbf{T}} \text{ on } \Gamma_s. \quad (16)$$

### 3. Fracture of compressible/incompressible hyperelastic materials

A general phase-field framework is outlined for the crack propagation modeling at large strains in hyperelastic materials. We then show the energy decomposition strategy for the unconstrained Ogden law to determine the component of strain energy that really contributes to crack growth. The damage degradation method is then modified by coupling with the proposed decomposition method. We present and prove that the incompressibility and nonnegativeness can be satisfied simultaneously by introducing the assumed strain method.

#### 3.1. Phase field modeling of crack propagation

Motivated by the idea of (Loew et al., 2019; Miehe et al., 2010; Tanné et al., 2018), the internal cracks in a solid can be approximated by the time- and space-dependent phase-field variable in a domain  $\Omega_0$

$$\psi \equiv \begin{cases} \Omega_0 \times \mathbb{T} \rightarrow [0, 1] \\ (\mathbf{X}, t) \mapsto \psi(\mathbf{X}, t) \end{cases} \quad (17)$$

The energy function of the crack surface can be described as

$$\Gamma_\ell(\psi) = \int_{\Omega_0} \gamma(\psi, \nabla \psi) d\Omega_0 = \int_{\Omega_0} \left( \frac{\psi^2}{2\ell} + \frac{\ell}{2} |\nabla \psi|^2 \right) d\Omega_0, \quad (18)$$

which regularizes the sharp cracks as diffusive fracture surfaces with phase-field variable  $\psi$  and its gradient  $\nabla \psi$ .

Then the variation of the function  $\Gamma_\ell(\psi)$  yields the Euler equation of the phase-field variable:

$$\begin{cases} \psi - \ell^2 \Delta \psi = 0 \text{ in } \Omega_0, \\ \nabla \psi \cdot \mathbf{N} = 0 \text{ on } \partial\Omega_0. \end{cases} \quad (19)$$

In order to understand the physical meaning of the diffused crack which controlled by phase-field variable intuitively, the one-dimensional analytical solution of Eq. (19) is given as  $\psi(x) = e^{-\frac{|x|}{\ell}}$ . The parameter  $\ell$  is the length scale parameter, which controls the width of the diffused crack, as shown in Fig. 2. To formulate the phase-deformation coupled multi-field framework, the mechanical driving force  $H_\psi$  shall be embedded into the model. Thus, the crack source term  $Y_\ell$  and the crack resistance term  $\Lambda_\ell$  is introduced as

$$\begin{cases} Y_\ell = \frac{1}{\ell} \int_{\Omega_0} (1 - \psi) H_\psi \cdot \dot{\psi} d\Omega_0, \\ \Lambda_\ell = \frac{1}{\ell} \int_{\Omega_0} \eta \dot{\psi} \cdot \dot{\psi} d\Omega_0. \end{cases} \quad (20)$$

$Y_\ell$  and  $\Lambda_\ell$  are combined to describe the crack evolution  $\dot{\Gamma}_\ell(\psi)$  within the time range  $\tau \in \mathbb{R}^+$ :

$$\dot{\Gamma}_\ell(\psi) = Y_\ell - \Lambda_\ell. \quad (21)$$

According to Eq. (18), its explicit mathematical expression is given as

$$\dot{\Gamma}_\ell(\psi) = \frac{1}{\ell} \int_{\Omega_0} (\psi - \ell^2 \Delta \psi) \cdot \dot{\psi} d\Omega_0. \quad (22)$$

Substituting Eq. (20) in Eq. (21), the equilibrium equation that governs the evolution is obtained as follows:

$$\psi - \ell^2 \Delta \psi = (1 - \psi) H_\psi - \eta \dot{\psi}. \quad (23)$$

The viscous resistance term  $\eta \dot{\psi}$  is usually added to improve the numerical robustness. Particularly, in rate-dependent problems and dynamic/quasi-static problems solved by the explicit scheme,  $\eta \dot{\psi}$  must be included as a time-integral term. However, in the quasi-static problem solved by implicit scheme,  $\eta \dot{\psi}$  can be omitted.

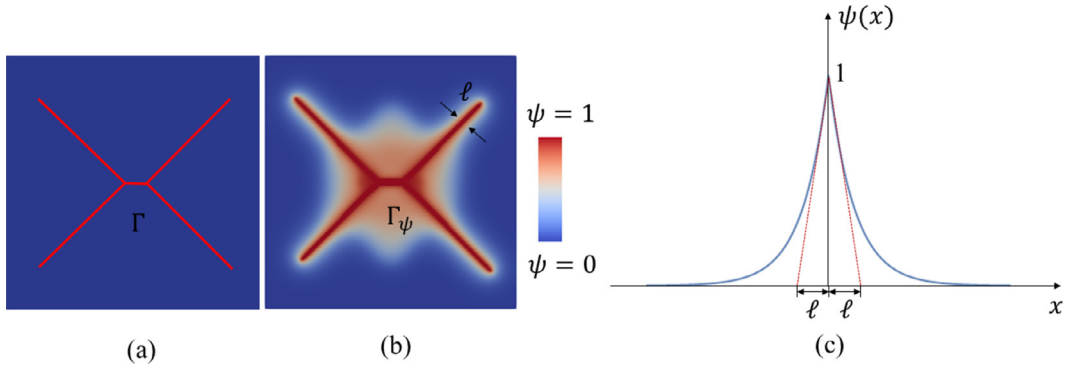


**Fig. 2.** (a) Solid with a sharp crack in topology discontinuity  $\Gamma$ , and (b) a diffusive crack  $\Gamma_\psi$  regularized by phase-field variable  $\psi$ . The red and blue regions represent the fully broken material (crack,  $\psi=1$ ) and the intact material ( $\psi=0$ ), respectively. Between the two areas is the diffusive transition zone ( $\psi \in (0, 1)$ ). (c) Phase-field variable  $\psi$  as a function of spatial coordinate:  $\psi(x) = e^{-\frac{|x|}{\ell}}$ .

Finally, to ensure the irreversibility of crack evolution, the mechanical driving force  $H_\psi$  is set as the maximum of the crack-driven state function  $\tilde{\Theta}$ , assessed over the entire time range  $\tau \in [0, t]$

$$H_\psi(\psi, t) = \max_{\tau \in [0, t]} \tilde{\Theta}(\mathbf{X}, \tau) \text{ with } \tilde{\Theta}(\mathbf{X}, \tau) \geq 0. \quad (24)$$

Here,  $\tilde{\Theta}$  is the crack-driven state function and defined as

$$\tilde{\Theta} = \frac{2\tilde{\Psi}}{G_c/\ell}, \quad (25)$$

which depends on the strain energy  $\tilde{\Psi}$ , critical fracture energy release rate  $G_c$ , and length scale parameter  $\ell$ .

### 3.2. Compressible/incompressible hyperelasticity coupled with phase-field model

#### 3.2.1. Strain energy decomposition on Ogden hyperelasticity

An unconstrained Ogden constitutive law (Ogden, 1997) takes the form as

$$\tilde{\Psi} = \tilde{\Psi}_{vol} + \tilde{\Psi}_{dev} = \frac{1}{2} \kappa \left( \frac{1}{2} (J^2 - 1) - \ln J \right) + \sum_{a=1}^{N_{ogd}} \left[ \frac{c_a}{m_a^2} \left( \sum_{i=1}^{SD} (\lambda_i^{m_a} - 1) - m_a \ln J \right) \right], \quad (26)$$

in which  $\tilde{\Psi}_{vol}$  is the volumetric energy and  $\tilde{\Psi}_{dev}$  is the deviatoric energy.  $\lambda_i (i = 1, \dots, SD)$  represents the arithmetic squared principal stretches of the right Cauchy-Green deformation tensor. It is essentially a statistic average of microscopic response of polymer network to tensile and compressive load at a typical point of the continuum, thereby reflects the equivalent deformation of micro structures.  $c_a$  and  $m_a (a = 1, 2, \dots, N_{ogd})$  are Ogden parameters. Here,  $N_{ogd}$  represents the number of terms of the Ogden parameters, which is determined by the polynomial fitting of experimental data.  $\kappa$  is the bulk modulus, when related to Ogden parameters  $c_a$  and Poisson's ratio  $\nu$ , satisfies

$$\kappa = \sum_{a=1}^{N_{ogd}} c_a \left( \frac{1}{3} + \beta_a \right) \text{ with } \beta_a = \frac{2\nu}{1-2\nu}, a = 1, 2, \dots, N_{ogd}, \quad (27)$$

In order to determine the component of strain energy that really contributes to crack growth, both the volumetric energy  $\tilde{\Psi}_{vol}$  and deviatoric energy  $\tilde{\Psi}_{dev}$  must be recomposed into active component  $\tilde{\Psi}_{act}$  and passive component  $\tilde{\Psi}_{pas}$ , where  $\tilde{\Psi}_{act}$  represents the crack-driven energy and  $\tilde{\Psi}_{pas}$  has no contribution.

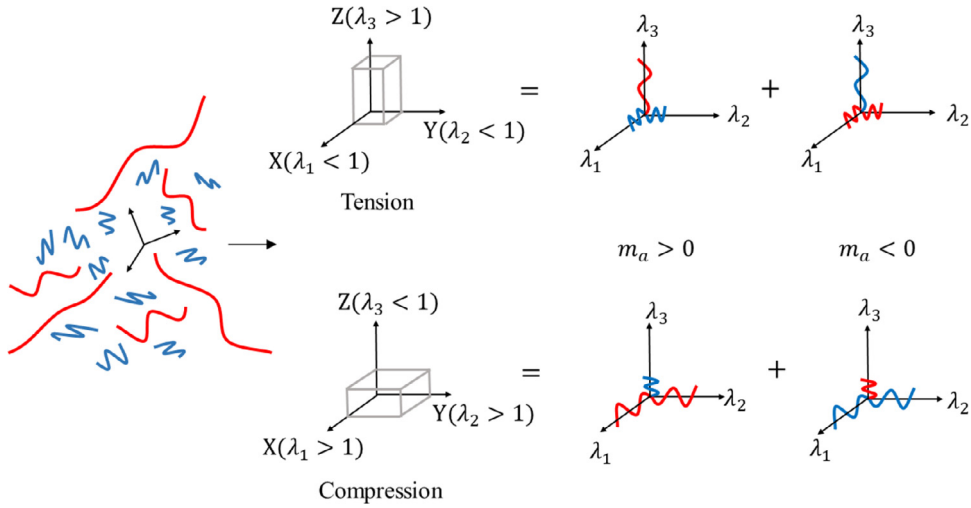


**Fig. 3.** Schematic of mechanical response to tension and compression at material point  $\mathbf{X} \in \Omega_0$ . The red and blue springs denote tensile stretches and compressive stretches, respectively.

Inspired by Borden et al. (2016), Miehe et al. (2010) and Tang et al. (2019), we decompose the strain energy as follows, however, with critical differences in the choice of the free energy:

$$\left\{ \begin{array}{l} \text{For } J \geq 1 : \\ \tilde{\Psi}^{act} = \sum_{i=1}^{SD} H(\lambda_i - 1) \sum_{a=1}^{N_{ogd}} \frac{c_a}{m_a^2} (\lambda_i^{m_a} - 1 - m_a \ln \lambda_i) + \frac{1}{2} \kappa \left( \frac{1}{2} (J^2 - 1) - \ln J \right), \\ \tilde{\Psi}^{pas} = \sum_{i=1}^{SD} H(1 - \lambda_i) \sum_{a=1}^{N_{ogd}} \frac{c_a}{m_a^2} (\lambda_i^{m_a} - 1 - m_a \ln \lambda_i), \\ \text{For } J < 1 : \\ \tilde{\Psi}^{act} = \sum_{i=1}^{SD} H(\lambda_i - 1) \sum_{a=1}^{N_{ogd}} \frac{c_a}{m_a^2} (\lambda_i^{m_a} - 1 - m_a \ln \lambda_i), \\ \tilde{\Psi}^{pas} = \sum_{i=1}^{SD} H(1 - \lambda_i) \sum_{a=1}^{N_{ogd}} \frac{c_a}{m_a^2} (\lambda_i^{m_a} - 1 - m_a \ln \lambda_i) + \frac{1}{2} \kappa \left( \frac{1}{2} (J^2 - 1) - \ln J \right), \\ \text{where } H(x) = \begin{cases} 1, & x \geq 0. \\ 0, & x < 0. \end{cases} \end{array} \right. \quad (28)$$

Here, the  $H(x)$  is Heaviside step function. We advance our above decomposition method to distinguishing tensile from compressive deformation along the principal axes at the material point  $\mathbf{X} \in \Omega_0$  (see Fig. 3), and eliminates the influence of signs of Ogden parameter  $m_a$  on the nonnegativeness of strain energy. Different from the aforementioned strategy, the influence of the parameters of material on the tensile and compressive properties of the strain energy is considered in our decomposition. From Eq. (28), there is no doubt that  $\frac{c_a}{m_a^2} (\lambda_i^{m_a} - 1 - m_a \ln \lambda_i)$  in the case of  $\lambda_i > 1$ ,  $m_a > 0$  represents the

stored energy caused by tension, which contributes to the active component  $\tilde{\Psi}^{act}$ . In the case of  $\lambda_i < 1$ ,  $m_a < 0$ , although  $\lambda_i < 1$ , the relative energy  $\frac{c_a}{m_a^2} (\lambda_i^{m_a} - 1 - m_a \ln \lambda_i)$  called pseudo-tension energy is equivalent to that when  $\lambda_i > 1$ ,  $m_a > 0$

mathematically, but it does not contribute to active component  $\tilde{\Psi}^{act}$  because it is caused by compressed stretches. The present energy decomposition provides a mathematical description about the change in the internal energy of the polymer chains due to tension and compression. By using our method, the strain energy of Ogden elastomer at multiaxial stress states will be distinguished accurately by accounting the characteristic of deformation along the individual axes. This could be a significant improvement over the conventional volumetric-deviatoric energy decomposition method.

### 3.2.2. Modified damage degradation method within strain energy decomposition

The material degradation induced by crack growth can be described by the damage degradation method in assuming that the internal energy  $W_{int}$  consists of degrading strain energy  $W_{def}$  and crack surface energy  $W_{frac}$ . Recall Eqs. (18) and



$$\begin{aligned}
K &= \begin{bmatrix} \dots & \dots & \dots & \dots & \dots \\ \dots & \dots & \dots & \dots & \dots \\ \dots & \varepsilon & \varepsilon & \varepsilon & \dots \\ \dots & \dots & \dots & \dots & \dots \\ \dots & \dots & \dots & \dots & \dots \end{bmatrix} & K_{\text{mod}} = \begin{bmatrix} \dots & \dots & \dots & \dots & \dots \\ \dots & \dots & \dots & \dots & \dots \\ \dots & \varepsilon + k_{\text{passive}} & \varepsilon + k_{\text{passive}} & \varepsilon + k_{\text{passive}} & \dots \\ \dots & \dots & \dots & \dots & \dots \\ \dots & \dots & \dots & \dots & \dots \end{bmatrix} \\
&\text{Singular matrix(ill-conditioned)} & \text{Nonsingular matrix(well-conditioned)}
\end{aligned}$$

**Fig. 4.**  $K$  and  $K_{\text{mod}}$  indicate the tangent stiffness matrix in unmodified method (no energy decomposition) and energy decomposition method, respectively.

(26),  $W_{\text{int}}$  is given as follows:

$$W_{\text{int}}(\mathbf{F}, \psi, \nabla \psi) = W_{\text{def}}(\mathbf{F}, \psi) + W_{\text{frac}}(\psi, \nabla \psi) = [(1 - \psi)^2 + \varepsilon] \tilde{\Psi} + G_c \left( \frac{\psi^2}{2\ell} + \frac{\ell}{2} |\nabla \psi|^2 \right). \quad (29)$$

Here,  $(1 - \psi)^2 + \varepsilon$  is the degradation function (Sargado et al., 2018), and  $\varepsilon$  is a small constant to maintain numerical stability, is taken as  $\varepsilon = 1 \times 10^{-6}$ . Combined with the energy decomposition expressed in Eq. (28), the internal energy  $W_{\text{int}}$  becomes

$$W_{\text{int}}(\mathbf{F}, \psi, \nabla \psi) = [(1 - \psi)^2 + \varepsilon] \tilde{\Psi}^{\text{act}} + \tilde{\Psi}^{\text{pas}} + G_c \left( \frac{\psi^2}{2\ell} + \frac{\ell}{2} |\nabla \psi|^2 \right), \quad (30)$$

and the crack-driven function in Eq. (25) is updated to a modified state function of

$$\tilde{\Theta} = \frac{2\tilde{\Psi}^{\text{act}}}{G_c/\ell}. \quad (31)$$

This formulation is essentially reflecting the physical reality that the molecular chain of hyperelastic material at microscopic level is quite flexible, thus the damage and fracture of hyperelastic material can only be induced by the energy change of the stretched molecular chains rather than the compressed molecular chains. The above modified damage degradation method can be regarded as a statistical average and continuum formulation of the damage and fracture of the microscopic polymer network.

**Remark 1.** (Mechanical degradation method coupled with strain energy decomposition): The above modified damage degradation method resolved the issue of numerical instability induced by material softening with relatively large deformation. As the material begins to soften, i.e. the phase-field variable  $\psi$  approaches 1, the material destabilizes, and the tangent stiffness matrix would become singular and produce huge negative eigenvalues, possibly resulting in the failure to approach the real solution. Applying the present energy decomposition method, the phase-field variable is only coupled with the active component  $\tilde{\Psi}^{\text{act}}$ , while the remaining passive part  $\tilde{\Psi}^{\text{pas}}$  reduces the singularity of the tangent stiffness matrix and makes the modified matrix  $K_{\text{mod}}$  well-conditioned (see Fig. 4). It is noted that the modified damage degradation method provides a universal description for the realistic material failure process, which progresses from damage to softening to fracture.

The instability problem has not been shown in the previous fracture at small strains because its governing equations are essentially linear, and no iteration is required. Hence, the convergence of the linear problems is not affected by the decomposition of strain energy.

### 3.2.3. Nonnegative prove of strain energy decomposition on incompressibility problem

The basic principle of energy decomposition is to guarantee the nonnegativeness of the strain energy, i.e.  $\tilde{\Psi}^{\text{act}} \geq 0$ ,  $\tilde{\Psi}^{\text{pas}} \geq 0$ , otherwise the numerical solution would not converge. The nonnegativeness of strain energy is indeed a constraint condition for fracture modeling to satisfy the second law of thermodynamics. For linear elastic materials, Hooke's law assures that no matter how the strain energy is decomposed, the component of strain energy  $\tilde{\Psi}_{\text{component}}$  can always be positive as following

$$\tilde{\Psi}_{\text{component}} = \frac{1}{2} \sigma_{\text{component}} : \varepsilon_{\text{component}} = \frac{1}{2} (\mathbf{C} : \varepsilon_{\text{component}}) : \varepsilon_{\text{component}} \geq 0 \forall \varepsilon_{\text{component}}, \quad (32)$$

where  $\sigma_{\text{component}}$  and  $\varepsilon_{\text{component}}$  are the Cauchy stress tensor and small strain tensor correspond to the  $\tilde{\Psi}_{\text{component}}$ , respectively. However, for nonlinear materials, the nonnegativeness of energy decomposition is dominated by the nonlinear incompressible constitutive law, such as Mooney-Rivlin law, of which the strain energy function takes the form as

$$\tilde{\Psi}_{M-R}(I_1, I_2) = C_1(I_1 - 3) + C_2(I_2 - 3) = C_1(\lambda_1^2 + \lambda_2^2 + \lambda_3^2 - 3) + C_2(\lambda_1^{-2} + \lambda_2^{-2} + \lambda_3^{-2} - 3). \quad (33)$$



Follow the present energy decomposition method, Mooney-Rivlin strain energy can be decomposed as

$$\begin{cases} \tilde{\Psi}^{act} = \sum_{i=1}^{SD} H(\lambda_i - 1) C_1 (\lambda_i^2 - 1) + \sum_{i=1}^{SD} H(\lambda_i - 1) C_2 (\lambda_i^{-2} - 1), \\ \tilde{\Psi}^{pas} = \sum_{i=1}^{SD} H(1 - \lambda_i) C_1 (\lambda_i^2 - 1) + \sum_{i=1}^{SD} H(1 - \lambda_i) C_2 (\lambda_i^{-2} - 1), \\ \text{where } H(x) = \begin{cases} 1, x \geq 0. \\ 0, x < 0. \end{cases} \end{cases} \quad (34)$$

where  $C_1$  and  $C_2$  are the material parameters, assumed to be  $> 0$  here. Two conclusions can be drawn from Eq (34): (i)  $\lambda_i > 1$  ( $i = 1, 2$ , and  $3$ ) holds only under triaxial tension. In another word,  $\lambda_i < 1$  ( $i = 1, 2$ , or  $3$ ) always hold for the other stress states, which leads to negative energy component:  $C_1 (\lambda_i^2 - 1) < 0$ . (ii) Polynomial exponents affect nonnegativeness, too. For example, even there is  $\lambda_i > 1$  ( $i = 1, 2, 3$ ), we still have  $C_1 (\lambda_i^{-2} - 1) < 0$  unless  $C_1 < 0$ . Thus, the incompressible constitutive law is impossible to be adopted in the present decomposition method to meet the requirement of nonnegativeness for incompressible fracture problems.

A contradiction arises from here: the present energy decomposition strategy is compatible with the actual fracture, but it cannot be applied in the modeling of incompressible materials due to the nonnegativeness condition is not meet automatically.

Now consider the unconstrained Ogden constitutive law used in this study, the volumetric strain energy  $\tilde{\Psi}_{vol}$  is non-negative apparently, thereby we will focus on the deviatoric strain energy  $\tilde{\Psi}_{dev}$ . The polar decomposition of the compatible deformation gradient  $\mathbf{F}$  in Eq. (2) is given as

$$\mathbf{F}|_{\mathbf{F}=\mathbf{1}+\mathbf{H}} = \mathbf{R}\mathbf{U} \text{ with } \mathbf{R}^T\mathbf{R} = \mathbf{1}, \mathbf{U} = \mathbf{U}^T, \quad (35)$$

where the  $\mathbf{R}$  and  $\mathbf{U}$  represent the compatible rotation tensor and compatible right stretch tensor, respectively. Subsequently, the decomposition of the compatible right Cauchy-Green deformation tensor  $\mathbf{C} = \mathbf{F}^T\mathbf{F}$  is formulated as

$$\mathbf{C} = \mathbf{U}^T\mathbf{R}^T \cdot \mathbf{R}\mathbf{U} = \mathbf{U}^T\mathbf{U} = \mathbf{U}^2. \quad (36)$$

Clearly, the compatible right Cauchy-Green deformation tensor  $\mathbf{C}$  is a positive definite matrix. Thus, its arithmetic squared principal stretches satisfy  $\lambda_i > 0$  ( $i = 1, \dots, SD$ ). Now, let us consider the component  $\Xi_i^a$  of the deviatoric energy  $\tilde{\Psi}_{dev}$  as

$$\begin{cases} \tilde{\Psi}_{dev} = \sum_{a=1}^{N_{ogd}} \sum_{i=1}^{N_{SD}} \Xi_i^a \\ \Xi_i^a = \frac{c_a}{m_a} (\lambda_i^{m_a} - 1 - m_a \ln \lambda_i) \text{ with } \lambda_i > 0, m_a \neq 0, i = 1, \dots, SD, a = 1, 2, \dots, N_{ogd}. \end{cases}, \quad (37)$$

with its derivative

$$\frac{d\Xi_i^a}{d\lambda_i} = \frac{c_a}{m_a} \frac{\lambda_i^{m_a} - 1}{\lambda_i}. \quad (38)$$

As illustrated in Fig. 5(a),  $\frac{d\Xi_i^a}{d\lambda_i}$  is always less than 0 when  $\lambda \in (0, 1)$ , while greater than 0 when  $\lambda \in [1, +\infty)$ , and equal to 0 when  $\lambda = 1$ . This property indicates that the minimum value of  $\Xi_i^a$  is always taken when  $\lambda = 1$ . It is noted that this relationship is independent of the signs and assignments of the Ogden parameter  $m_a$ , which is set as -3, -2, -1, 1, 2, 3, 4 for demonstration. It can be seen from Fig. 5(b) that the deviatoric energy component  $\Xi_i^a$  always has a minimum value 0 when  $\lambda = 1$  (no deformation), so  $\Xi_i^a > 0$  holds at any  $\lambda$ .

We prove that the unconstrained Ogden constitutive law is the unique hyperelastic energy description that meet the nonnegativeness of the deviatoric strain energy  $\tilde{\Psi}_{dev}$  during the present energy decomposition. In unconstrained Ogden law, the combination of the unconstrained term  $\ln \lambda_i$  and  $\lambda_i$  make  $\Xi_i^a$  being in a form of hyperbolic function with the minimum 0. Although the term  $\ln \lambda_i$  produces undesired pseudo-strain energy due to that the mapping relationship  $\nabla_{\mathbf{x}}\mathbf{x}$  between  $\Omega_0$  and  $\Omega_t$  does not meet the incompressibility constraint, we could introduce the enhanced deformation gradient  $\tilde{\mathbf{f}}$  to fix it (Fig. 6 (a)), as discussed in Section 2.2. The assumed strain essentially eliminates the undesired volumetric deformation such that the pseudo-strain energy produced by the unconstrained term  $\ln \lambda_i$  is also eliminated, thereby the unconstrained Ogden constitutive law can be applied to describe the mechanical response of incompressible material by introducing the assumed strain.

The next question is whether the requirement of nonnegativeness can still be satisfied after introducing the assumed strain. Following Hauptmann et al. (2000), the polar decomposition of the assumed deformation gradient  $\tilde{\mathbf{F}}$  in Eq. (12) is introduced as

$$\tilde{\mathbf{F}}|_{\tilde{\mathbf{F}}=\mathbf{1}+\tilde{\mathbf{H}}} = \tilde{\mathbf{R}}\tilde{\mathbf{U}}, \quad (39)$$

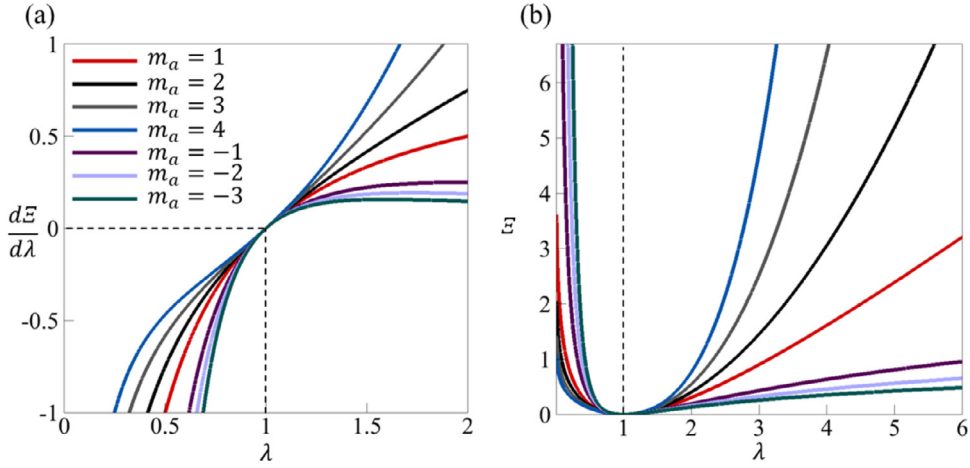


**Fig. 5.** Visualization of the deviatoric energy component  $\Xi$  and its derivative with the argument  $\lambda$ : (a) Curves of derivative of  $\Xi$  when  $m_a$  varies from  $-3$  to  $4$ ; (b) Curves of  $\Xi$  when  $m_a$  varies from  $-3$  to  $4$ .  $c_a = 1$  for simplicity.

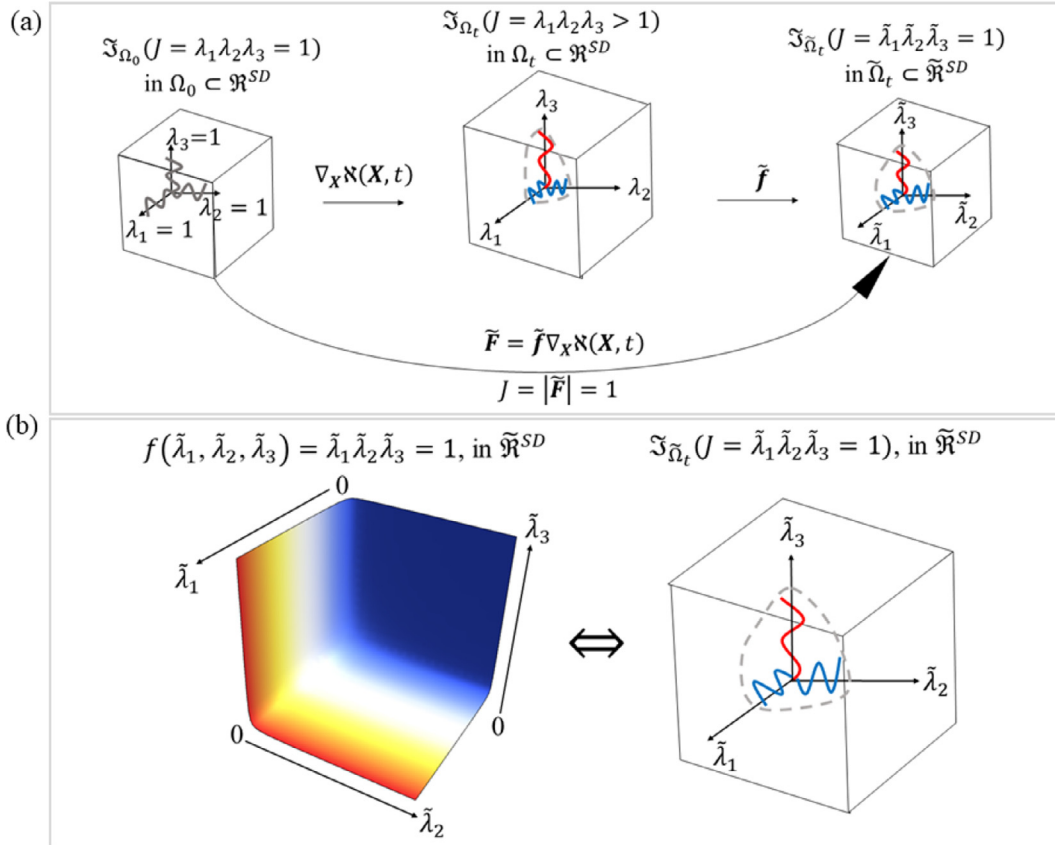


**Fig. 6.** Scheme of the assume strain method (a) Mapping  $\mathfrak{S}_{\Omega}$  to  $\mathfrak{S}_{\tilde{\Omega}}$  through the assumed deformation gradient  $\tilde{\mathbf{F}}$  to approximate the incompressible molecular network in the assumed strain space; (b) The mapping surface in assumed strain space represents all the possible deformation states of incompressible material.

where  $\tilde{\mathbf{R}}$  is an orthogonal matrix satisfying  $\tilde{\mathbf{R}}^T \tilde{\mathbf{R}} = \mathbf{1}$  and  $\tilde{\mathbf{U}}$  is still a symmetric matrix satisfying  $\tilde{\mathbf{U}}^T = \tilde{\mathbf{U}}$ . Subsequently, the decomposition of the assumed right Cauchy-Green deformation tensor  $\tilde{\mathbf{C}} = \tilde{\mathbf{F}}^T \tilde{\mathbf{F}}$  is formulated as

$$\tilde{\mathbf{C}} = \tilde{\mathbf{U}}^T \tilde{\mathbf{R}}^T \cdot \tilde{\mathbf{R}} \tilde{\mathbf{U}} = \tilde{\mathbf{U}}^T \tilde{\mathbf{U}} = \tilde{\mathbf{U}}^2. \quad (40)$$

As similar as  $\mathbf{C}$  in Eq. (36),  $\tilde{\mathbf{C}}$  is also a positive definite matrix, indicating that its arithmetic squared principal stretches satisfy  $\tilde{\lambda}_i > 0 (i = 1, \dots, SD)$ . Apparently, the nonnegativeness of  $\tilde{\lambda}_i$  ensures  $\tilde{\Xi}_i^a(\tilde{\lambda}_i) = \frac{c_a}{m_a}(\tilde{\lambda}_i^{m_a} - 1 - m_a \ln \tilde{\lambda}_i) \geq 0$ , which means the introduction of assumed strain does not affect the nonnegativeness of the deviatoric energy  $\tilde{\Psi}_{dev}$ , so that the present energy decomposition method can be applied to the incompressible problem as

$$\tilde{\Psi} = \tilde{\Psi}^{act}(\tilde{\lambda}_1, \tilde{\lambda}_2, \tilde{\lambda}_3) + \tilde{\Psi}^{pas}(\tilde{\lambda}_1, \tilde{\lambda}_2, \tilde{\lambda}_3) \text{ with } \tilde{\mathbf{C}} = \tilde{\mathbf{F}}^T \tilde{\mathbf{F}}|_{\tilde{\mathbf{F}}=\mathbf{1}+\mathbf{H}+\tilde{\mathbf{H}}} = \sum_{i=1}^{SD} \tilde{\lambda}_i^2 \mathbf{N}_i \otimes \mathbf{N}_i. \quad (41)$$

The surface  $f(\tilde{\lambda}_1, \tilde{\lambda}_2, \tilde{\lambda}_3)$  is a mathematical set of  $\tilde{\lambda}_i (i = 1, \dots, SD)$  in an assumed strain space  $\tilde{\mathfrak{R}}^{SD}$  (with  $SD \in \{1, 2, 3\}$ ) as shown in Fig. 6(b). Each point on the surface is related to one possible deformation state  $\mathfrak{S}_{\tilde{\Omega}_t}$  of the incompressible material. This surface approximates the deformation of the micromorphology of incompressible polymer, and only in the surface  $f(\tilde{\lambda}_1, \tilde{\lambda}_2, \tilde{\lambda}_3)$  the nonnegativeness within the present energy decomposition can be satisfied, which means the deformation represented by this surface is in consistent with the second law of thermodynamics.

## 4. Numerical implementation

### 4.1. The weak form of the multi-field fracture problem

In view of the weak form of Eqs. (15), (23) and (30) can be written as

$$\begin{cases} \int_{\Omega_0} \left[ 2[(1-\psi)^2 + \varepsilon] \frac{\partial \tilde{\Psi}^{act}}{\partial \tilde{\mathbf{C}}} \tilde{\mathbf{F}}^T + 2 \frac{\partial \tilde{\Psi}^{pas}}{\partial \tilde{\mathbf{C}}} \tilde{\mathbf{F}}^T \right] \delta(\nabla \mathbf{u}) + \rho_0 \mathbf{b}_0 \delta \mathbf{u} dV = 0, \\ \int_{\Omega_0} \left[ 2 \frac{\partial (\tilde{\Psi}^{act} + \tilde{\Psi}^{pas})}{\partial \tilde{\mathbf{C}}} \tilde{\mathbf{F}}^T - \mathbf{P} \right] \delta \tilde{\mathbf{H}} dV = 0, \\ \int_{\Omega_0} \delta \mathbf{P} \cdot \tilde{\mathbf{H}} dV = 0, \\ \int_{\Omega_0} (\ell^2 \nabla \psi \cdot \nabla \delta \psi + \psi \delta \psi + \eta \dot{\psi} \delta \psi) dV - \int_{\Omega_0} (1-\psi) H_\psi \delta \psi dV = 0, \end{cases} \quad (42)$$

with approximation spaces

$$\begin{cases} U = \{ \mathbf{u} \in C^0 | \mathbf{u} = \bar{\mathbf{u}} \text{ on } \partial \Omega_0 \}, \\ \mathcal{U} = \{ \delta \mathbf{u} \in C^0 | \delta \mathbf{u} = \mathbf{0} \text{ on } \partial \Omega_0 \}, \\ V = \{ \psi \in C^0 | \psi = \bar{\psi} \text{ on } \partial \Omega_0 \}, \\ \mathcal{V} = \{ \delta \psi \in C^0 | \delta \psi = 0 \text{ on } \partial \Omega_0 \}. \end{cases} \quad (43)$$

For compressible problems, the assumed strain field would not be evolved in the above formula, as a result the four-field scheme is shirked to the three-field scheme. For incompressible problem, the standard orthogonality condition (Simo and Rifai, 1990) is imposed between the assumed strain and stress fields such that the stress field drops out in the following formulation.

### 4.2. FEM discretization

Let  $\tilde{\mathcal{B}}^h = \cup_{e=1}^{N_{elem}} \tilde{\mathcal{B}}^e$  be a finite element discretization constructed by means of isoperimetric elements. The standard FEM defines the following approximations

$$\begin{cases} \mathbf{u}^h = \sum_{l=1}^{N_{node}} N^l(\boldsymbol{\xi}) \mathbf{d}_l^e, \delta \mathbf{u}^h = \sum_{l=1}^{N_{node}} N^l(\boldsymbol{\xi}) \delta \mathbf{d}_l^e, \\ \psi^h = \sum_{l=1}^{N_{node}} N^l(\boldsymbol{\xi}) \tilde{\psi}_l^e, \delta \psi^h = \sum_{l=1}^{N_{node}} N^l(\boldsymbol{\xi}) \delta \tilde{\psi}_l^e. \end{cases} \quad (44)$$

Here,  $N_{node}$  is the number of nodes of the element and  $N^l$  represents the finite element shape function associated with node  $l$ .  $\mathbf{d}_l^e$  and  $\tilde{\psi}_l^e (l = 1, 2, \dots, N_{node})$  are the displacement and phase-field at node  $l$ , respectively. Now let  $\mathbf{J}$  be the  $N_{SD} \times N_{SD}$  Jacobian matrix and let

$$\nabla_{\mathbf{X}} N^l := \left\{ \frac{\partial N^l}{\partial \mathbf{X}_A} \right\}_{A=1, \dots, N_{SD}}, \quad \nabla_{\boldsymbol{\xi}} N^l := \left\{ \frac{\partial N^l}{\partial \boldsymbol{\xi}_A} \right\}_{A=1, \dots, N_{SD}}. \quad (45)$$

Through the chain rule, the standard relation denotes

$$\mathbf{B}_l^u(\mathbf{X}) = \mathbf{J}^{-1} \nabla_{\boldsymbol{\xi}} N^l. \quad (46)$$

Consequently, the compatible displacement gradient  $\nabla \mathbf{u}_e^h$  and its variations restricted to  $\tilde{\mathcal{B}}^e$  is given by

$$\nabla \mathbf{u}^h = \sum_{l=1}^{N_{node}} \mathbf{d}_l^e \otimes \mathbf{B}_l^u, \quad \nabla \delta \mathbf{u}^h = \sum_{l=1}^{N_{node}} \delta \mathbf{d}_l^e \otimes \mathbf{B}_l^u, \quad (47)$$

which corresponds to the compatible part of the assumed deformation gradient  $\tilde{\mathbf{F}}$  in Eq. (12).

Similarly, the material gradient of phase-field variable and its variations are interpolated through the suitable operator as

$$\nabla \psi^h(\mathbf{X}, t) = \sum_{l=1}^{N_{node}} \mathbf{B}_l^\psi(\mathbf{X}) \tilde{\psi}_l(t), \quad \nabla \delta \psi^h(\mathbf{X}, t) = \sum_{l=1}^{N_{node}} \mathbf{B}_l^\psi(\mathbf{X}) \delta \tilde{\psi}_l(t). \quad (48)$$

The following interpolation is given for the enhanced displacement gradient  $\tilde{\mathbf{H}}$  and its variations  $\delta \tilde{\mathbf{H}}$ ,

$$\tilde{\nabla} N = \frac{\partial \tilde{N}}{\partial \tilde{\boldsymbol{\xi}}} = \left[ \frac{\partial \tilde{N}^1}{\partial \tilde{\boldsymbol{\xi}}}, \dots, \frac{\partial \tilde{N}^{N_{enh}}}{\partial \tilde{\boldsymbol{\xi}}} \right] = \tilde{\mathbf{J}}_0^{-1} \frac{\partial \tilde{N}}{\partial \boldsymbol{\xi}}, \quad \mathbf{X} \in \Omega_0, \quad (49)$$

where  $\tilde{\mathbf{J}}$  is the determinant of the Jacobian matrix  $\mathbf{J}$ .  $\mathbf{J}_0$  is the Jacobian matrix evaluated at the centroid of  $\tilde{\mathcal{B}}^e$ , and  $\tilde{\mathbf{J}}_0$  is its determinant. The  $\frac{\partial \tilde{N}}{\partial \tilde{\boldsymbol{\xi}}}$  is an  $N_{SD} \times N_{Nenh}$  matrix, defines as

$$\frac{\partial \tilde{N}}{\partial \tilde{\boldsymbol{\xi}}} = \begin{bmatrix} \xi & 0 & 0 \\ 0 & \eta & 0 \\ 0 & 0 & \zeta \end{bmatrix}, \quad (50)$$

for the three-dimensional brick element. This interpolation can be seen as an enhancement of the corresponding change in the center of the element. Then the enhanced displacement gradient  $\tilde{\mathbf{H}}$  and its variations  $\delta \tilde{\mathbf{H}}$  can be written as

$$\tilde{\mathbf{H}}_e = \sum_{l=1}^{N_{enh}} \boldsymbol{\beta}_l^e \otimes \mathbf{B}_l^\beta, \quad \delta \tilde{\mathbf{H}}_e = \sum_{l=1}^{N_{enh}} \delta \boldsymbol{\beta}_l^e \otimes \mathbf{B}_l^\beta, \quad (51)$$

where  $N_{enh}$  represents the assumed modes in the element and  $\boldsymbol{\beta}_l^e$  are  $N_{SD} \times N_{Nenh}$  local parameters. Finally, the finite element interpolation of the assumed deformation gradient  $\tilde{\mathbf{F}}$  can be written as

$$\tilde{\mathbf{F}}^h = \sum_{e=1}^{N_{elem}} \tilde{\mathbf{F}}_e, \quad \tilde{\mathbf{F}}_e = \mathbf{1} + \nabla \mathbf{u}_e^h + \tilde{\mathbf{H}}_e = \mathbf{1} + \sum_{l=1}^{N_{node}} \mathbf{d}_l^e \otimes \mathbf{B}_l^u + \sum_{l=1}^{N_{enh}} \boldsymbol{\beta}_l^e \otimes \mathbf{B}_l^\beta. \quad (52)$$

Substituting FE interpolation (47), (48), and (51) into the weak forms (42) lead the following discrete form

$$\begin{cases} \mathcal{A}_{e=1}^{N_{elem}} \left[ \mathbf{f}_e^{\mathbf{u},int}(\mathbf{u}_e, \boldsymbol{\beta}_e) - \mathbf{f}_e^{\mathbf{u},ext}(\mathbf{u}_e) \right] = 0, \\ \mathbf{f}_e^{\boldsymbol{\beta},int}(\mathbf{u}_e, \boldsymbol{\beta}_e) = 0, \text{ for } e = 1, 2, \dots, N_{elem}, \\ \mathcal{A}_{e=1}^{N_{elem}} \mathbf{f}_e^{\psi,int}(\psi_e, \nabla \psi_e) = 0, \end{cases} \quad (53)$$

in which  $\mathcal{A}$  is the element assembly operator. Specifically, the inner force vector  $\mathbf{f}_e^{\mathbf{u},int}$  and the external force vector  $\mathbf{f}_e^{\mathbf{u},ext}$  of the displacement field, the inner force vector  $\mathbf{f}_e^{\boldsymbol{\beta},int}$  of the local parameters field, the inner force vector  $\mathbf{f}_e^{\psi,int}$  of the phase-field are described by

$$\begin{cases} \mathbf{f}_e^{\mathbf{u},int} = \int_{\Omega_0^e} \mathbf{B}_e^{\mathbf{u}T} \left[ 2[(1-\psi)^2 + \varepsilon] \frac{\partial \tilde{\Psi}^{act}}{\partial \tilde{\mathbf{C}}} \tilde{\mathbf{F}}^T + 2 \frac{\partial \tilde{\Psi}^{pas}}{\partial \tilde{\mathbf{C}}} \tilde{\mathbf{F}}^T \right] d\Omega_0^e, \\ \mathbf{f}_e^{\mathbf{u},ext} = \int_{\Omega_0^e} \mathbf{N}_e^{\mathbf{u}T} \mathbf{b}_0^e d\Omega_0^e + \int_{\Gamma_s} \mathbf{N}_e^{\mathbf{u}T} \bar{\mathbf{T}}_0^e d\Gamma_0^e, \\ \mathbf{f}_e^{\boldsymbol{\beta},int} = \int_{\Omega_0^e} \mathbf{B}_e^{\boldsymbol{\beta}T} \left[ 2[(1-\psi)^2 + \varepsilon] \frac{\partial \tilde{\Psi}^{act}}{\partial \tilde{\mathbf{C}}} \tilde{\mathbf{F}}^T + 2 \frac{\partial \tilde{\Psi}^{pas}}{\partial \tilde{\mathbf{C}}} \tilde{\mathbf{F}}^T \right] d\Omega_0^e, \\ \mathbf{f}_e^{\psi,int} = \int_{\Omega_0^e} \left[ (\ell^2 \mathbf{B}_e^{\psi T} \nabla \psi + \mathbf{N}_e^{\psi T} \psi) - (1-\psi) \mathbf{N}_e^{\psi T} H_\psi + \mathbf{N}_e^{\psi T} \eta \psi \right] d\Omega_0^e. \end{cases} \quad (54)$$

The Eq. (42)<sub>3</sub> indicates the interelement discontinuity of the interpolation (51) holds individually for each element of the mesh. Within a Newton-Raphson iterative scheme for solution of the nonlinear system (53), this property gives rise to a static condensation procedure whereby the interactive increment of the local parameters  $\boldsymbol{\beta}$  is determined at the element level for each iteration and the linearized Eqs. (53)<sub>1</sub> and (53)<sub>2</sub> to be solved at the global level is reduced to a displacement-like format. Since the phase-field variable  $\psi$  and the displacement field  $\mathbf{u}$  are coupled by  $H_\psi$  which related to the strain energy, a standard staggered multi-field finite element scheme is established.

## 5. Results and discussion

We highlight in this section the capability of the developed phase-field framework to model crack propagation of compressible and incompressible hyperelastic materials by experiment and three representative examples. The first two examples of compressible rubbery materials under uniaxial and biaxial tension are investigated to validate the proposed energy

**Table 1**

Material parameters used in the numerical simulation

Examples	$N_{ogd}$	$\frac{C_1}{m_1}$ (MPa)	$m_1$	$\frac{C_2}{m_2}$ (MPa)	$m_2$	$\frac{C_3}{m_3}$ (MPa)	$m_3$	$\nu$	$G_c$ (N/mm)	$\ell$ (mm)
5.1	3	0.66	1.3	0.0012	5	-0.01	-2	0.455	4.0	5.0
5.2	3	0.66	1.3	0.0012	5	-0.01	-2	0.455	4.0	1.0
5.3	2	0.1562	2	-0.1096	-2	\	\	0.499	1.87	5.0

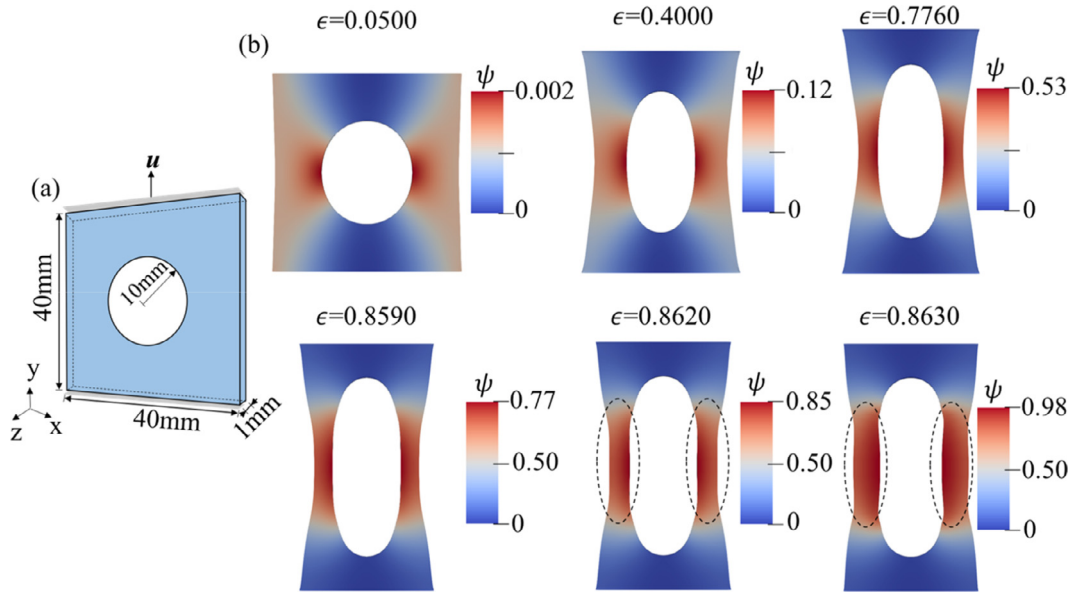


**Fig. 7.** Uniaxial tension on the circular pre-cracked hyperelastic plate. (a) Geometry and boundary conditions. (b) Crack patterns in various fracture stages of  $u = 2.00, 16.00, 26.00, 31.04, 34.36, 34.48, 34.52$  mm by using the ASPFM.  $\epsilon$  represents the nominal strain.

decomposition method for fracture modeling. Tensile experiment on silicone rubber is designed and implemented to verify our numerical prediction on the crack growth at large strain. As the third benchmark example, we focus on the fracture of incompressible hyperelasticity in the geometry of double edge notched specimen that allows to further validation by comparison with experimental results.

Material parameters are used as same as Ogden (1997) and Hocine et al. (2002) to facilitate validation study, as listed in Table 1. The mesh adopted in simulations has been subjected to convergence analysis and refined where the crack initialization and propagation are expected. The code of numerical implementation is written by Fortran and the visualization is performed by ParaView.

### 5.1. Fracture in hyperelastic plate with hole under uniaxial tension: hole collapse effect

As a first benchmark example, we consider a square plate of length 40 mm, containing a circular hole in the center with a radius of 10 mm under uniaxial tension, as depicted in Fig. 7(a). The bottom boundary of the specimen is fixed, while the top boundary changes subject to vertical displacement.

The crack patterns predicted by the developed assumed strain phase-field coupled method (ASPFM) are shown in Fig. 7(b). It can be seen that the final values of the phase-field variable  $\psi$  are close to 1 when  $\epsilon$  arrives 0.8630, indicating that ASPFM successfully captures the crack growth under uniaxial tension. From the final fracture period, noted that when nominal strain  $\epsilon$  increases only 0.1% from 0.8620 to 0.8630, the phase-field variable  $\psi$  will increase quickly from 0.85 to nearly 1, indicating that sudden fracture could be triggered under a tiny increment of load at large strain. Therefore, the numerical prediction of fracture failure of rubbery materials is quite sensitive to loading rate, which should be decreased at large strain to guarantee the accurate prediction of crack propagation. In this study, the strain rate is set to be  $1.00 \times 10^{-4}$  s.

Furthermore, ASPFM captures an interesting phenomenon at large strain ( $\epsilon = 0.863$ ) as illustrated in Fig. 7(b), that is, the circular hole contracting inward around the crack tip. To verify the simulated phenomenon, qualitative experiments are designed for characterization. A silicon rubber specimen is prepared with geometry identical to that in the simulation. The uniaxial tensile test is implemented by MTS, and the quasi-static loading conditions are assured by setting the loading rate to  $1.33 \times 10^{-4}$  m/s. The entire loading process lasts for 202.5 s. For comparison, we also implement the crack prediction using micro-mechanically based phase-field model (MMPFM) in Miehe and Schaezel (2014) and the volumetric-deviatoric decomposition phase-field model (VDPFM) in Wu et al. (2016). The comparison results of the experiment and numerical

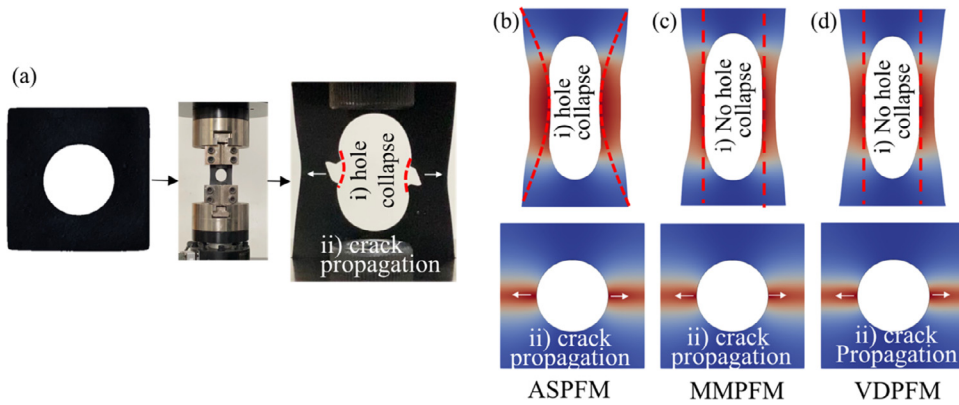


**Fig. 8.** Crack propagation and the hole collapse effect observed from experiment and captured by different models. (a) Tension test on the silicon rubber specimen with a circular hole; (b) Predicted final crack pattern with “hole collapse effect” in the current configuration, and reference configuration with crack propagation by ASPFM; (c) Predicted final failed pattern in the current and reference configuration by MMPFM; (d) Predicted final failed pattern in the current and reference configuration by VDPFM.

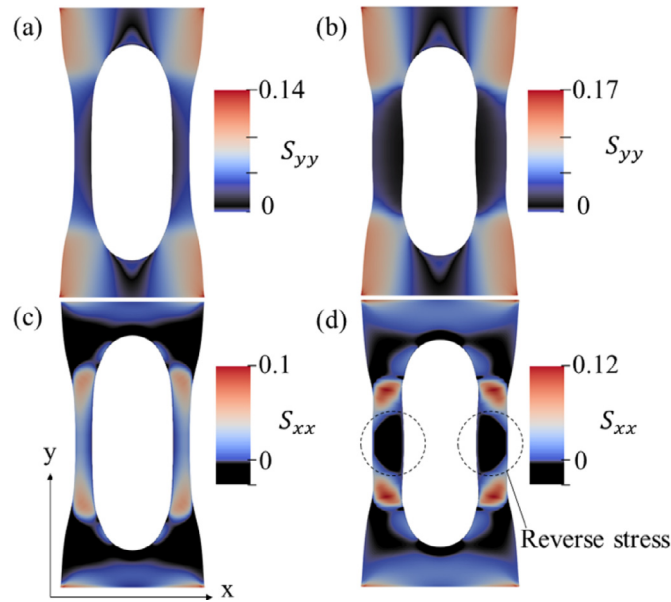


**Fig. 9.** Distributions of second Piola-Kirchhoff stress in the final failed pattern. (a)  $S_{yy}$  by the MMPFM; (b)  $S_{yy}$  by the ASPFM; (c)  $S_{xx}$  by the MMPFM; (d)  $S_{xx}$  by the ASPFM.

results predicted by ASPFM, MMPFM and VDPFM are shown in Fig. 8. It can be seen from the experimental result that as the cracks propagate, the circular hole around the crack tip contracted inward significantly, as shown in Fig. 8(a).

From Fig. 8(b)–(d), all the three models predict crack growth along  $x$  direction consistently, however, the phenomenon of “Hole Collapse Effect” (HCE) can be only captured by ASPFM (see Fig. 8(b)), which is also observed from the experiment. But using MMPFM and VDPFM, the edges of the circular hole appear to maintain a straight form (see Fig. 8(c) and (d)). HCE can be viewed as a unique effect along with finite deformation fractures of hyperelastic materials. The underlying mechanics would be that when the fracture of the polymer network is taken to occur, many molecular chains rupture simultaneously. As a result, chains in the high stress area are unable to resist tensile deformation but exhibits cohesive slip. This dynamic response of molecular chains can be statistically characterized in terms of second Piola-Kirchhoff stress distribution at the crack tip, as shown in Fig. 9, where the area of  $S_{yy} = 0$  and  $S_{xx} < 0$  are blackened. The second Piola-Kirchhoff stress distribution in the final failed pattern predicted by MMPFM is calculated for reference. Clearly, MMPFM generates residual tensile stress  $S_{yy}$  around the crack tip under large deformation, and the residual stress prevents the hole from contracting inward. However, in the distribution predicted by ASPFM, the  $S_{yy}$  can be zero around the crack tip, leading to the release from tensile stress along the  $y$  direction. To meet the requirement of overall static balance, the reverse stress  $S_{xx}$  is generated automatically around the crack tip, and eventually leads to the HCE (see Fig. 9(d)). Based on the results, we demonstrate that



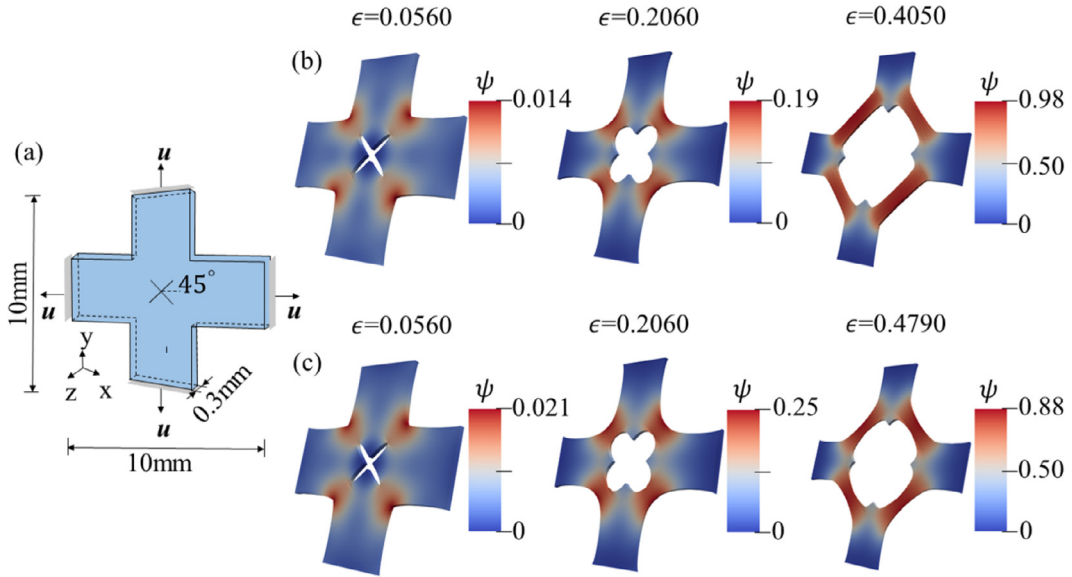


**Fig. 10.** Biaxial tension test on the hyperelastic material. (a) Geometry and boundary conditions; (b) Crack patterns in various fracture stages of  $u = 0.56, 2.06, 4.05$  mm predicted by ASPFM. (c) Crack patterns in various fracture stages of  $u = 0.56, 2.06, 4.79$  mm predicted by MMPFM.  $\epsilon$  represents the nominal strain.

the ASPFM provides a statistical average for the motion of molecular chains as the damage and deformation are increased to substantial levels, which is rarely captured by the other model.

### 5.2. Crack propagation on pre-cracked specimen under biaxial tension

To gain further insight into ASPFM, the fracture of hyperelastic material in the case of biaxial tension is simulated. The geometry of the specimen and the applied boundary conditions are depicted in Fig. 10(a).

The crack patterns obtained by using the present model and MMPFM under biaxial tension are depicted in Fig. 10(b) and (c). Using MMPFM model, the phase-field variable  $\psi$  fails to reach 1 when full fracture almost happens, due to that the numerical instability and computing collapse caused by material softening is magnified in the complex stress state. This numerical problem can be eliminated by the developed energy decomposition model, which reduces the matrix singularity and significantly improves the computational stability (refer to Section 3.2.2), thus leading to the accurate result that the phase-field variable  $\psi$  is quite close to 1.

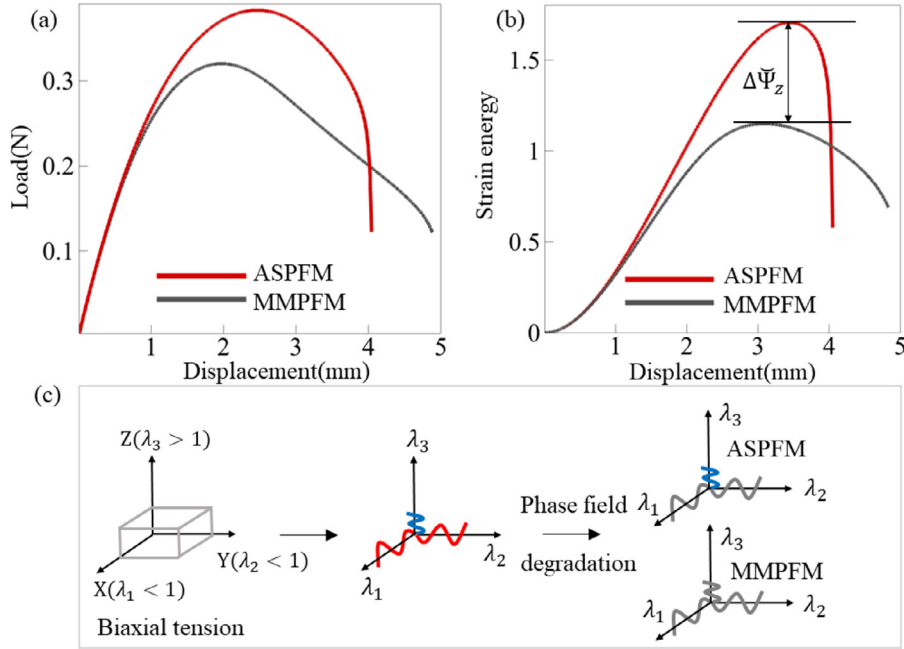
We explore the main differences between the two models by the displacement-load curves (see Fig. 11 (a)). First, MMPFM reaches the critical strength faster as it assumes that all the strain energy contributes to the crack growth, leading to a significant acceleration in the phase-field simulation, and underestimation of the critical strength than the true value. However, ASPFM accounts reasonably for the energy that actually contributes to the fracture, which effectively eliminates the deviation in the prediction of critical strength. Second, after reaching the critical strength, the material tends to be softening for a prolonged period by MMPFM, without occurrence of fracture failure until the end of the calculation. But obviously fracture failure can be captured by ASPFM after a short period of softening. This can be interpreted by the loss of strain energy. As shown in Fig. 11(c), biaxial tension deformation can be equivalent to a three-axis tensile and compressive model, where the principal stretches on the axes  $x$  and  $y$  are in a tensed state, and the axis  $z$  is in a compressed state. In ASPFM, the phase-field damage function is only coupled with the deformation in  $x$  and  $y$  direction rather than coupled with all the directions in MMPFM. The latter will result in the loss of the  $z$ -axial strain energy (Fig. 11(b)). Then the decreased strain energy is insufficient to generate new crack surface, so the material maintains softening.

Fig. 12(a) shows the response of the second Piola–Kirchhoff stress  $S_{xy}$ , which plays a primary role in the softening process. It can be seen that, in the ASPFM, the shear stress  $S_{xy}$  undergoes a sharp drop after reaching the critical strength, indicating that the material has undergone local shear softening. The evolution of shear stress  $S_{xy}$  is plotted in Fig. 12(b), corresponding to the different stages in Fig. 12(a). At stages (I) and (II), the shear stress  $S_{xy}$  is concentrated at the crack tip and increases such that the initial notches are blunted at  $45^\circ$ . The nucleation and propagation of the cracks are associated with a sudden jump to 0 of the shear stress  $S_{xy}$  around crack tips towards stage (III).

### 5.3. Fracture in incompressible hyperelastic material

The Fracture in incompressible hyperelastic materials have been experimentally conducted on double edge notched in tension (Hocine et al., 2002). The styrene butadiene rubber specimen of 200 mm length and 80 mm width were made from





**Fig. 11.** Failure characteristics of hyperelastic materials captured by ASPFM and MMPFM. (a) Displacement-Load curves; (b) Displacement-Strain energy curves; (c) Schematic illustration of biaxial tensile failure by an equivalent three-axis tensile and compressive model. Red and blue springs denote tensile stretches and compressive stretches respectively. Grey spring denote the damage stretches dominated by phase-field. (For interpretation of the references to color in this figure legend, the reader is referred to the web version of this article.)

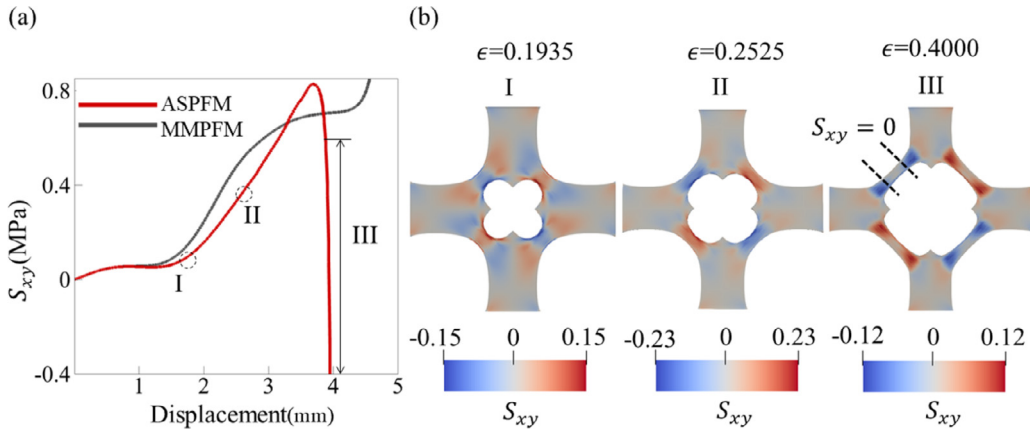


**Fig. 12.** Shear stress evolution under biaxial tension. (a) Evolution of the second Piola-Kirchhoff stress  $S_{xy}$  with the displacement; (b) Distributions of second Piola-Kirchhoff stress  $S_{xy}$  in the various stages of fracture failure.  $\epsilon$  represents the nominal strain.

a rubber sheet of 3 mm thickness, the length of the two initial notches is 28 mm. The Mooney-Rivlin law for nearly incompressible hyperelastic materials was adopted to describe the mechanical behavior in the study. Based on experimental results, various numerical frameworks are well-established to understand the fracture failure of the incompressible problems (Miehe and Schaezel, 2014; Tang et al., 2019; Wu et al., 2016) by deriving equivalent compressible material parameters from the micromechanical quantities of the polymer network of incompressible rubbers, and working on the compressible problem instead of solving incompressible problem directly. However, as the incompressible constitutive law is usually complicated, over-simplification on it will lead to loss in accuracy and limitation in engineering applicability.

In ASPFM, the assumed strain method is introduced to meet the incompressibility constraint conditions. The formulation establishes an equivalent conversion between the incompressible Mooney-Rivlin law adopted in experiment and the present unconstrained Ogden law. Such that the incompressible material parameters obtained in the experiment can be directly applied in the fracture prediction by using unconstrained Ogden constitutive law. Here the simulations are compared to experimental measurements with the same geometry, as shown in Fig. 13(a).

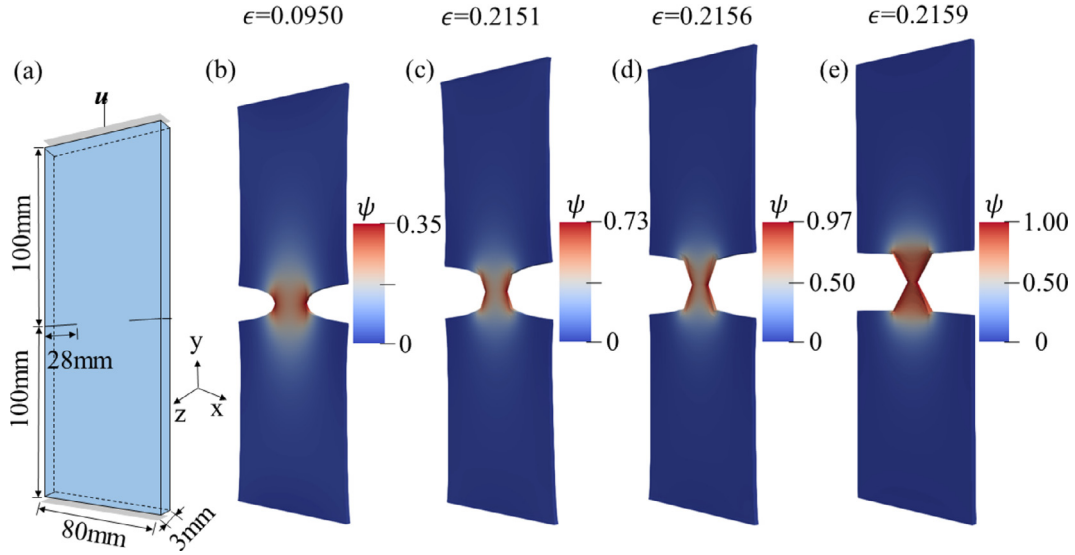


**Fig. 13.** Double-edge notched bar under tensile test. (a) Geometry and boundary conditions; Crack pattern in various fracture stages: (b)  $u = 19.00$  mm; (c)  $u = 43.04$  mm; (d)  $u = 43.13$  mm; (e)  $u = 43.18$  mm.  $\epsilon$  represents the nominal strain.

**Remark 2.** (Equivalent conversion): The Mooney–Rivlin law can be regarded as a binomial form of the unconstrained Ogden law under incompressible constraint. Thus, the two constitutive relationships can be equivalent to each other as follows.

The Mooney–Rivlin strain energy function for incompressible hyperelastic materials is given as

$$\tilde{\Psi}_{M-R}(I_1, I_2) = C_1(I_1 - 3) + C_2(I_2 - 3). \quad (55)$$

Because of incompressibility, i.e.  $\lambda_1\lambda_2\lambda_3 = 1$ , Eq. (55) can be reformulated as

$$\tilde{\Psi}_{M-R}(\lambda_1, \lambda_2, \lambda_3) = C_1(\lambda_1^2 + \lambda_2^2 + \lambda_3^2 - 3) + C_2(\lambda_1^{-2} + \lambda_2^{-2} + \lambda_3^{-2} - 3). \quad (56)$$

Owing to that the assumed strain always meets incompressible constraint, the unconstrained Ogden law can be equivalent to the Mooney–Rivlin law by setting

$$\begin{aligned} m_1 &= 2, \\ m_2 &= 2, \\ \frac{c_1}{m_1} &= 2C_1, \\ \frac{c_2}{m_2} &= -2C_2. \end{aligned} \quad (57)$$

For the bulk modulus  $\kappa$ , any large value that similar to the incompressible material is to be taken.

To be noted, the developed equivalent conversion can be extended to any polynomial hyperelastic constitutive laws under incompressible constraint conditions, which is of great help to practical engineering problems. In this study, we converse Mooney–Rivlin law to the unconstrained Ogden law because the latter can meet the nonnegativeness as required in the energy decomposition.

The visualization of the crack opening and the crack growth in the deformation configuration is shown in Fig. 13(b)–(e). A small damage zone appears at the notch tip when the specimen is stretched to  $\epsilon = 0.0950$ . In the subsequent splitting process under further stretch, the damage zones grow larger and propagate inward, eventually interact with each other, as shown in Fig. 13(e).

A set of numerical load-displacement responses using various method are compared to the experimental results, as depicted in Fig. 14 (a). The approximated result obtained by ASPFM is highly consistent with the experimental results. One reason is that ASPFM accounts strain energy that actually contributes to crack growth. Another is that the developed assumed strain method effectively reduces pseudo-strain energy produced by incompressibility and maintains the stability of finite element simulation. The incompressibility of elastomers is originally from the van der Waals interaction between adjacent molecules chains in polymer network. As shown in Fig. 15, The compatible deformation gradient  $\nabla_{\mathbf{X}}\mathbf{N}(\mathbf{X}, \mathbf{t})$  can be mapped into the assumed strain space to achieve  $J = \tilde{\lambda}_1\tilde{\lambda}_2\tilde{\lambda}_3 = 1$ . The obtained mapping surface under uniaxial tension is the mathematical approximation of polymer networks in the assumed strain space, which contains all the potential states at uniaxial tensile deformation.

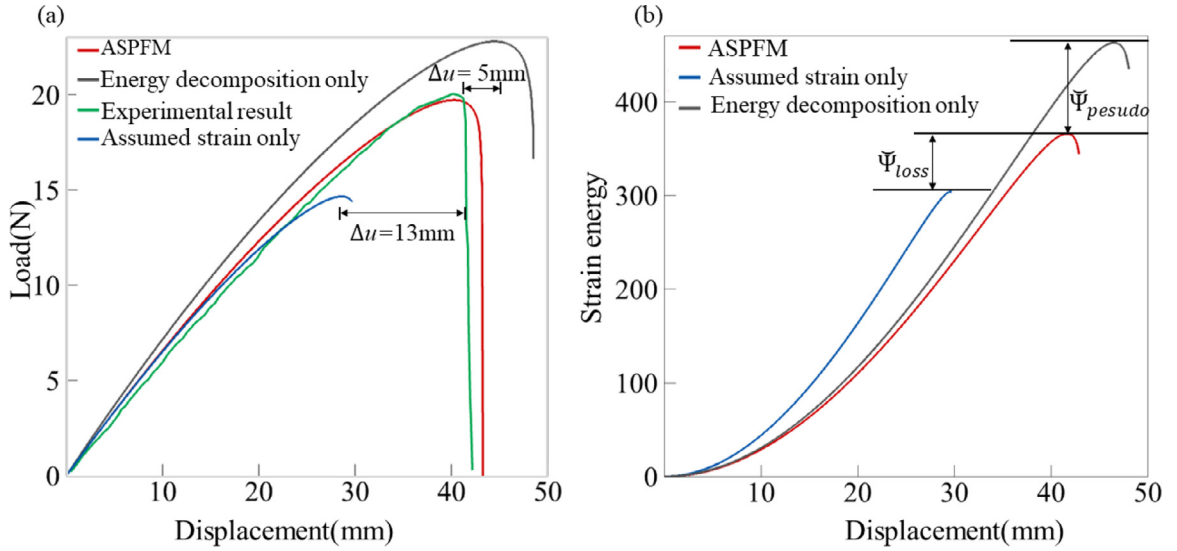


Fig. 14. (a) Numerical and experimental load-displacement responses. (b) Displacement-Strain energy curves.

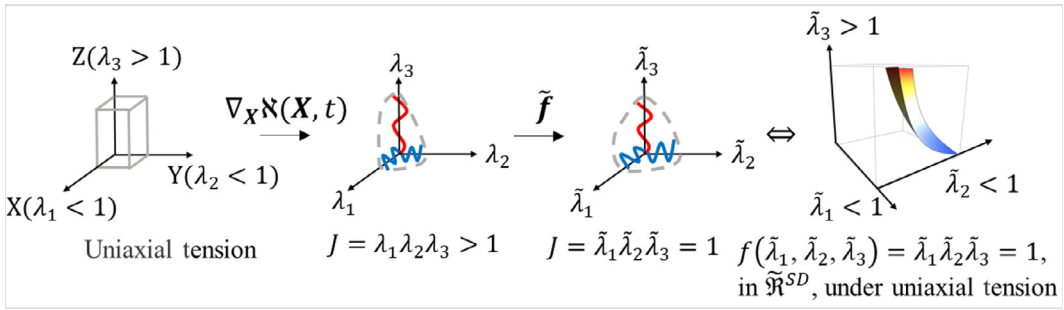


Fig. 15. The mathematical approximation of incompressible material in the assumed strain space under uniaxial tension

Thereafter we will demonstrate the significance of the assumed strain model in large-scale fracture simulation of incompressible materials. Without embedding the assumed strain in the energy decomposition, the incompressibility constraint does not hold, leading to pseudo-strain energy that does not really contribute to the crack growth. As shown in Fig. 14(a), applying the model that only employs energy decomposition, the displacement at critical strength is 5 mm larger than the relative experimental result. The difference in the estimation of displacement-load curve is due to the pseudo-strain energy  $\Psi_{pseudo}$  been counted in the applied model (Fig. 14(b)), leading to overestimation of the strength than the material really has. In another case, using the model only accounts assumed strain, the predicted critical strength is much smaller than the experimental data. This difference is caused by the energy loss in the computation that prevents the material from reaching its true critical strength. As discussed earlier in Section 5.2, the material softening is taken to start but cannot continue, due to the numerical instability of the discussed model. Furthermore, compared with compressible material, the fracture modeling on incompressible problem is much sensitive to the numerical instability. It is noted that the present phase-field model by Eq. (30) is sensitive to the length scale parameter  $\ell$ . In order to show this effect, the load-displacement curves in different  $\ell$  are simulated and presented in Fig. 16. From the results, larger  $\ell$  leads to lower nominal critical strength but almost the same critical displacement. On this issue, Wu and Vinh Phu (2018) have proposed a length scale insensitive phase-field model for linear elastic materials, and the length scale insensitive phase-field model for hyperelastic materials would be discussed in our future work.

Finally, in order to further track the incompressibility constraint by the ASPFM, we investigate the evolution of the volume expansion ratio during fracture. From Fig. 17, we demonstrate that the material is nearly incompressible prior to crack nucleation and propagation by the ASPFM. As the cracks begin to propagate, the volume expansion ratio enlarges dramatically. This trend is quantitatively consistent with the finding of Li and Bouklas (2020), though they conduct uniaxial tension on different hyperelastic materials.

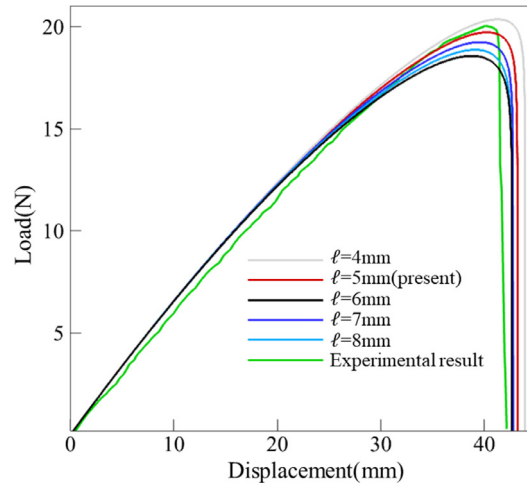


Fig. 16. load-displacement responses in different length scale parameter  $\ell$  and comparing with the experimental result (Hocine et al., 2002).

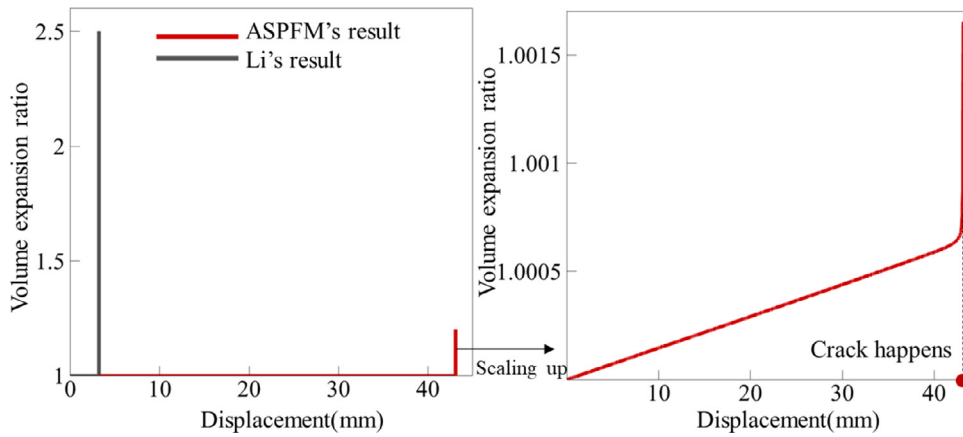


Fig. 17. Volume expansion of incompressible materials before and after fracture by comparing the present results with Li's results.

## 6. Conclusions

An advanced phase-field model (ASPFM), which accounts for the coupled effects of the stretches, damage and incompressibility in hyperelastic materials, is formulated. Different from the most phase-field models that focus on the validation of crack propagation path, the model pays attention to the mechanical response of the material during fracture through three benchmark tests. The main conclusions of the study are as follows:

- (i) Compared to the experimental crack patterns, the uniaxial tensile test on a compressible hyperelastic plate with a central hole shows that ASPFM is able to capture the interesting phenomenon, that is, the effect of hole collapse.
- (ii) Biaxial tension on the X-shape compressible specimen shows that ASPFM resolve the issue of numerical instability caused by material softening effectively, making it capable to simulate the whole failure progresses from damage to softening to fracture.
- (iii) Uniaxial tension test on the double edge notched specimen of incompressible styrene butadiene rubber illustrates that ASPFM can reproduce the macroscopic load-displacement characteristics and predicted the critical material strength accurately during the fracture failure.

The good agreement between the results from the present simulations and the experiment indicates that the developed model should be of practical utility in optimizing the fracture-resistant design of hyperelastic material products.

In this study, the interpolation of the enhanced displacement gradient  $\tilde{\mathbf{H}}$  remains an issue that need to be addressed. From Fig. 17, it can be seen that the incompressibility constraints are not strictly ensured, because the interpolation in Eq. (50) is not effective enough to eliminate the volume deformation completely. It would be worthwhile in the future to devise a more efficient interpolation for the enhanced displacement gradient  $\tilde{\mathbf{H}}$ .

## Declaration of Competing Interest

The authors declare that they have no known competing financial interests or personal relationships that could have appeared to influence the work reported in this paper.

## CRediT authorship contribution statement

**Jia-Yu Ye:** Methodology, Formal analysis, Writing - original draft, Investigation. **Lu-Wen Zhang:** Methodology, Writing - review & editing, Supervision. **J.N. Reddy:** Writing - review & editing.

## Acknowledgments

The work is supported by [Natural Science Foundation of Shanghai](#) (Grant No. 19ZR1474400) and [National Natural Science Foundation of China](#) (Grant No. 11872245). The authors thank Mr. Bin-Bin Yin for the discussion and constructive suggestions.

## Appendix. Incremental update algorithm

We use a staggered update scheme to solve Eq. (53) algorithmically. The linearization of the element vectors  $\mathbf{f}_e^{\mathbf{u},int}$  and  $\mathbf{f}_e^{\psi,int}$ , concerning the intermediate solution  $(\mathbf{u}_e^k, \beta_e^k, \psi_e^k)$ , takes the form

$$\begin{cases} \text{Linear} \left[ \mathbf{f}_e^{\mathbf{u},int} \right] = \mathbf{f}_e^{\mathbf{u},k} + \mathbf{k}_e^{\mathbf{uu},k} \Delta \mathbf{u}_e + \mathbf{k}_e^{\mathbf{u}\beta,k} \Delta \beta_e = 0, \\ \text{Linear} \left[ \mathbf{f}_e^{\beta,int} \right] = \mathbf{f}_e^{\beta,k} + \mathbf{k}_e^{\beta\mathbf{u},k} \Delta \mathbf{u}_e + \mathbf{k}_e^{\beta\beta,k} \Delta \beta_e = 0, \\ \text{Linear} \left[ \mathbf{f}_e^{\psi,int} \right] = \mathbf{f}_e^{\psi,k} + \mathbf{k}_e^{\psi\psi,k} \Delta \psi_e = 0, \end{cases} \quad (\text{A-1})$$

where a superscript  $k$  indicates evaluation at the known intermediate  $k_{th}$  solution step. The update is divided into two steps. In the first solution step an update for the degrees of freedom related to displacement and assumed strain field is performed and the crack phase-field  $\psi$  is hold constant. In view of Eq. (42)<sub>3</sub>, the linearized equation of (A-1)<sub>1</sub> and (A-1)<sub>2</sub> can be solved at the element level for  $\Delta \beta_e$

$$\Delta \beta_e = - \left( \mathbf{k}_e^{\beta\beta,k} \right)^{-1} \left( \mathbf{f}_e^{\beta,k} + \mathbf{k}_e^{\beta\mathbf{u},k} \Delta \mathbf{u}_e \right). \quad (\text{A-2})$$

This procedure called static condensation, yields an enhanced displacement-like equation which, after assembly, can be written in the standard form

$$\bar{\mathbf{K}}_{\mathbf{uu}}^k \Delta \mathbf{u} = \bar{\mathbf{R}}_{\mathbf{uu}}^k, \quad (\text{A-3})$$

where

$$\begin{cases} \bar{\mathbf{K}}_{\mathbf{uu}}^k = \mathcal{A}_{e=1}^{n_{elem}} \left[ \mathbf{k}_e^{\mathbf{uu}} - \mathbf{k}_e^{\mathbf{u}\beta} \left( \mathbf{k}_e^{\beta\beta} \right)^{-1} \mathbf{k}_e^{\beta\mathbf{u}} \right]^k, \\ \bar{\mathbf{R}}_{\mathbf{uu}}^k = \mathcal{A}_{e=1}^{n_{elem}} \left[ \mathbf{f}_e^{\mathbf{u},ext} - \mathbf{f}_e^{\mathbf{u},int} + \mathbf{k}_e^{\mathbf{u}\beta} \left( \mathbf{k}_e^{\beta\beta} \right)^{-1} \mathbf{f}_e^{\beta,int} \right]^k. \end{cases} \quad (\text{A-4})$$

In the above equation, we further have

$$\begin{cases} \mathbf{k}_e^{\mathbf{uu}} = \int_{\Omega_0^e} \mathbf{B}_{e0}^T \left[ 4[(1-\psi)^2 + \varepsilon] \frac{\partial^2 \tilde{\Psi}^{act}}{\partial \tilde{\mathbf{C}}^2} + 4 \frac{\partial^2 \tilde{\Psi}^{pas}}{\partial \tilde{\mathbf{C}}^2} \right] \mathbf{B}_{e0} d\Omega_0^e + \mathbf{k}_e^{\mathbf{uu},geom} \otimes \mathbf{1}, \\ \mathbf{k}_e^{\mathbf{u}\beta} = \int_{\Omega_0^e} \mathbf{B}_{e0}^T \left[ 4[(1-\psi)^2 + \varepsilon] \frac{\partial^2 \tilde{\Psi}^{act}}{\partial \tilde{\mathbf{C}}^2} + 4 \frac{\partial^2 \tilde{\Psi}^{pas}}{\partial \tilde{\mathbf{C}}^2} \right] \mathbf{B}_{e0}^{\beta} d\Omega_0^e + \mathbf{k}_e^{\mathbf{u}\beta,geom} \otimes \mathbf{1}, \\ \mathbf{k}_e^{\beta\mathbf{u}} = \int_{\Omega_0^e} \mathbf{B}_{e0}^T \left[ 4[(1-\psi)^2 + \varepsilon] \frac{\partial^2 \tilde{\Psi}^{act}}{\partial \tilde{\mathbf{C}}^2} + 4 \frac{\partial^2 \tilde{\Psi}^{pas}}{\partial \tilde{\mathbf{C}}^2} \right] \mathbf{B}_{e0}^{\mathbf{u}} d\Omega_0^e + \mathbf{k}_e^{\beta\mathbf{u},geom} \otimes \mathbf{1}, \\ \mathbf{k}_e^{\beta\beta} = \int_{\Omega_0^e} \mathbf{B}_{e0}^T \left[ 4[(1-\psi)^2 + \varepsilon] \frac{\partial^2 \tilde{\Psi}^{act}}{\partial \tilde{\mathbf{C}}^2} + 4 \frac{\partial^2 \tilde{\Psi}^{pas}}{\partial \tilde{\mathbf{C}}^2} \right] \mathbf{B}_{e0}^{\beta} d\Omega_0^e + \mathbf{k}_e^{\beta\beta,geom} \otimes \mathbf{1}, \end{cases} \quad (\text{A-5})$$

where  $\mathbf{1}$  is an  $N_{SD} \times N_{SD}$  identity matrix. The geometric part of tangent matrix is given by

$$\begin{cases} \mathbf{K}_e^{\mathbf{uu},\text{geom}} = \int_{\Omega_0^e} \nabla_{\mathbf{x}} N^T \left[ 2[(1-\psi)^2 + \varepsilon] \frac{\partial \tilde{\Psi}^{\text{act}}}{\partial \tilde{\mathbf{C}}} + 2 \frac{\partial \tilde{\Psi}^{\text{pas}}}{\partial \tilde{\mathbf{C}}} \right] \nabla_{\mathbf{x}} N d\Omega_0^e, \\ \mathbf{K}_e^{\mathbf{u}\beta,\text{geom}} = \int_{\Omega_0^e} \nabla_{\mathbf{x}} N^T \left[ 2[(1-\psi)^2 + \varepsilon] \frac{\partial \tilde{\Psi}^{\text{act}}}{\partial \tilde{\mathbf{C}}} + 2 \frac{\partial \tilde{\Psi}^{\text{pas}}}{\partial \tilde{\mathbf{C}}} \right] \tilde{\nabla}_{\mathbf{x}} N d\Omega_0^e, \\ \mathbf{K}_e^{\beta\mathbf{u},\text{geom}} = \int_{\Omega_0^e} \tilde{\nabla}_{\mathbf{x}} N^T \left[ 2[(1-\psi)^2 + \varepsilon] \frac{\partial \tilde{\Psi}^{\text{act}}}{\partial \tilde{\mathbf{C}}} + 2 \frac{\partial \tilde{\Psi}^{\text{pas}}}{\partial \tilde{\mathbf{C}}} \right] \nabla_{\mathbf{x}} N d\Omega_0^e, \\ \mathbf{K}_e^{\beta\beta,\text{geom}} = \int_{\Omega_0^e} \tilde{\nabla}_{\mathbf{x}} N^T \left[ 2[(1-\psi)^2 + \varepsilon] \frac{\partial \tilde{\Psi}^{\text{act}}}{\partial \tilde{\mathbf{C}}} + 2 \frac{\partial \tilde{\Psi}^{\text{pas}}}{\partial \tilde{\mathbf{C}}} \right] \tilde{\nabla}_{\mathbf{x}} N d\Omega_0^e. \end{cases} \quad (\text{A-6})$$

The interpolation matrix is given by

$$\mathbf{B}_{e0,ijkl}^{\mathbf{u}} = \text{sym}_{(i,j)} \left( \frac{\partial N^I}{\partial X_i} \tilde{F}_{kj} \right), \quad \mathbf{B}_{e0,ijkl}^{\beta} = \text{sym}_{(i,j)} \left( \frac{\partial \tilde{N}^I}{\partial X_i} \tilde{F}_{kj} \right). \quad (\text{A-7})$$

Here the Voigt form can be expressed by

$$\mathbf{B}_{e0,I}^{\mathbf{u}} = \begin{bmatrix} \frac{\partial N^I}{\partial X} \frac{\partial \tilde{x}}{\partial X} \frac{\partial N^I}{\partial X} \frac{\partial \tilde{y}}{\partial X} \frac{\partial N^I}{\partial X} \frac{\partial \tilde{z}}{\partial X} \\ \frac{\partial N^I}{\partial Y} \frac{\partial \tilde{x}}{\partial Y} \frac{\partial N^I}{\partial Y} \frac{\partial \tilde{y}}{\partial Y} \frac{\partial N^I}{\partial Y} \frac{\partial \tilde{z}}{\partial Y} \\ \frac{\partial N^I}{\partial Z} \frac{\partial \tilde{x}}{\partial Z} \frac{\partial N^I}{\partial Z} \frac{\partial \tilde{y}}{\partial Z} \frac{\partial N^I}{\partial Z} \frac{\partial \tilde{z}}{\partial Z} \\ \frac{\partial N^I}{\partial Y} \frac{\partial \tilde{x}}{\partial Z} + \frac{\partial N^I}{\partial Z} \frac{\partial \tilde{x}}{\partial Y} \frac{\partial N^I}{\partial Y} \frac{\partial \tilde{y}}{\partial Z} + \frac{\partial N^I}{\partial Z} \frac{\partial \tilde{y}}{\partial Y} \frac{\partial N^I}{\partial Y} \frac{\partial \tilde{z}}{\partial Z} + \frac{\partial N^I}{\partial Z} \frac{\partial \tilde{z}}{\partial Y} \\ \frac{\partial N^I}{\partial X} \frac{\partial \tilde{x}}{\partial Z} + \frac{\partial N^I}{\partial Z} \frac{\partial \tilde{x}}{\partial X} \frac{\partial N^I}{\partial X} \frac{\partial \tilde{y}}{\partial Z} + \frac{\partial N^I}{\partial Z} \frac{\partial \tilde{y}}{\partial X} \frac{\partial N^I}{\partial X} \frac{\partial \tilde{z}}{\partial Z} + \frac{\partial N^I}{\partial Z} \frac{\partial \tilde{z}}{\partial X} \\ \frac{\partial N^I}{\partial X} \frac{\partial \tilde{x}}{\partial Y} + \frac{\partial N^I}{\partial Y} \frac{\partial \tilde{x}}{\partial X} \frac{\partial N^I}{\partial X} \frac{\partial \tilde{y}}{\partial Y} + \frac{\partial N^I}{\partial Y} \frac{\partial \tilde{y}}{\partial X} \frac{\partial N^I}{\partial X} \frac{\partial \tilde{z}}{\partial Y} + \frac{\partial N^I}{\partial Y} \frac{\partial \tilde{z}}{\partial X} \end{bmatrix}, \quad (\text{A-8})$$

$$\mathbf{B}_{e0,I}^{\beta} = \begin{bmatrix} \frac{\partial \tilde{N}^I}{\partial X} \frac{\partial \tilde{x}}{\partial X} \frac{\partial \tilde{N}^I}{\partial X} \frac{\partial \tilde{y}}{\partial X} \frac{\partial \tilde{N}^I}{\partial X} \frac{\partial \tilde{z}}{\partial X} \\ \frac{\partial \tilde{N}^I}{\partial Y} \frac{\partial \tilde{x}}{\partial Y} \frac{\partial \tilde{N}^I}{\partial Y} \frac{\partial \tilde{y}}{\partial Y} \frac{\partial \tilde{N}^I}{\partial Y} \frac{\partial \tilde{z}}{\partial Y} \\ \frac{\partial \tilde{N}^I}{\partial Z} \frac{\partial \tilde{x}}{\partial Z} \frac{\partial \tilde{N}^I}{\partial Z} \frac{\partial \tilde{y}}{\partial Z} \frac{\partial \tilde{N}^I}{\partial Z} \frac{\partial \tilde{z}}{\partial Z} \\ \frac{\partial \tilde{N}^I}{\partial Y} \frac{\partial \tilde{x}}{\partial Z} + \frac{\partial \tilde{N}^I}{\partial Z} \frac{\partial \tilde{x}}{\partial Y} \frac{\partial \tilde{N}^I}{\partial Y} \frac{\partial \tilde{y}}{\partial Z} + \frac{\partial \tilde{N}^I}{\partial Z} \frac{\partial \tilde{y}}{\partial Y} \frac{\partial \tilde{N}^I}{\partial Y} \frac{\partial \tilde{z}}{\partial Z} + \frac{\partial \tilde{N}^I}{\partial Z} \frac{\partial \tilde{z}}{\partial Y} \\ \frac{\partial \tilde{N}^I}{\partial X} \frac{\partial \tilde{x}}{\partial Z} + \frac{\partial \tilde{N}^I}{\partial Z} \frac{\partial \tilde{x}}{\partial X} \frac{\partial \tilde{N}^I}{\partial X} \frac{\partial \tilde{y}}{\partial Z} + \frac{\partial \tilde{N}^I}{\partial Z} \frac{\partial \tilde{y}}{\partial X} \frac{\partial \tilde{N}^I}{\partial X} \frac{\partial \tilde{z}}{\partial Z} + \frac{\partial \tilde{N}^I}{\partial Z} \frac{\partial \tilde{z}}{\partial X} \\ \frac{\partial \tilde{N}^I}{\partial X} \frac{\partial \tilde{x}}{\partial Y} + \frac{\partial \tilde{N}^I}{\partial Y} \frac{\partial \tilde{x}}{\partial X} \frac{\partial \tilde{N}^I}{\partial X} \frac{\partial \tilde{y}}{\partial Y} + \frac{\partial \tilde{N}^I}{\partial Y} \frac{\partial \tilde{y}}{\partial X} \frac{\partial \tilde{N}^I}{\partial X} \frac{\partial \tilde{z}}{\partial Y} + \frac{\partial \tilde{N}^I}{\partial Y} \frac{\partial \tilde{z}}{\partial X} \end{bmatrix}, \quad (\text{A-9})$$

where  $N^I$  represents the finite element shape function associated with node  $I$  ( $I = 1, 2, \dots, N_{\text{node}}$ ) and  $\tilde{N}^I$  represents the finite element shape function associated with the assumed modes  $I$  ( $I = 1, 2, \dots, N_{\text{nenh}}$ ). Eq. (A-3) can be solved by repeating

$$\begin{cases} \mathbf{u}_e^{k+1} = \mathbf{u}_e^k + \Delta \mathbf{u}_e, \\ \boldsymbol{\beta}_e^{k+1} = \boldsymbol{\beta}_e^k + \Delta \boldsymbol{\beta}_e, \end{cases} \quad \text{for } e = 1, 2, \dots, N_{\text{elem}}, \quad (\text{A-10})$$

until the convergence conditions  $\left\{ \begin{array}{l} \|\mathbf{u}_e^{k+1} - \mathbf{u}_e^k\| < \text{tol} \\ \|\boldsymbol{\beta}_e^{k+1} - \boldsymbol{\beta}_e^k\| < \text{tol} \end{array} \right.$  are satisfied. In the second step the displacement and assumed strain field are hold constant. Eq. (A-1)<sub>3</sub> is solved to obtain the phase-field variable  $\psi$ , its solution scheme is given as

$$\mathbf{K}_{\psi\psi}^k \Delta \psi = \mathbf{R}_{\psi\psi}^k, \quad (\text{A-11})$$

where

$$\begin{cases} \mathbf{K}_{\psi\psi}^k = \mathcal{A}_{e=1}^{n_{elem}} [\mathbf{k}_e^{\psi\psi}]^k, \\ \mathbf{R}_{\psi\psi}^k = \mathcal{A}_{e=1}^{n_{elem}} [-\mathbf{f}_e^{u,int}]^k. \end{cases} \quad (\text{A-12})$$

Here

$$\mathbf{k}_e^{\psi\psi} = \int_{\Omega_0^e} \left[ \mathbf{B}_e^{\psi T} \ell^2 \mathbf{B}_e^{\psi} + \mathbf{N}_e^{\psi T} \mathbf{N}_e^{\psi} \left( \frac{\eta}{\tau} + H_{\psi} + 1 \right) \right] d\Omega_0^e \quad (\text{A-13})$$

where  $\tau$  is the time increment. Eq. (A-11) can be solved by repeating

$$\psi_e^{k+1} = \psi_e^k + \Delta \psi_e, \text{ for } e = 1, 2, \dots, N_{elem}, \quad (\text{A-14})$$

until  $\|\psi_e^{k+1} - \psi_e^k\| < tol$  is achieved.

## References

- Areias, P., Msekh, M.A., Rabczuk, T., 2016a. Damage and fracture algorithm using the screened Poisson equation and local remeshing. *Eng. Fract. Mech.* 158, 116–143.
- Areias, P., Rabczuk, T., Msekh, M.A., 2016b. Phase-field analysis of finite-strain plates and shells including element subdivision. *Comput. Methods Appl. Mech. Eng.* 312, 322–350.
- Azevedo, N.M., Lemos, J.V., 2006. Hybrid discrete element/finite element method for fracture analysis. *Comput. Methods Appl. Mech. Eng.* 195, 4579–4593.
- Borden, M.J., Hughes, T.J.R., Landis, C.M., Anvari, A., Lee, I.J., 2016. A phase-field formulation for fracture in ductile materials: Finite deformation balance law derivation, plastic degradation, and stress triaxiality effects. *Comput. Methods Appl. Mech. Eng.* 312, 130–166.
- Borden, M.J., Verhoosel, C.V., Scott, M.A., Hughes, T.J.R., Landis, C.M., 2012. A phase-field description of dynamic brittle fracture. *Comput. Methods Appl. Mech. Eng.* 217, 77–95.
- Bourdin, B., Francfort, G.A., Marigo, J.J., 2000. Numerical experiments in revisited brittle fracture. *J. Mech. Phys. Solids* 48, 797–826.
- Boyce, M.C., Arruda, E.M., 2000. Constitutive models of rubber elasticity: a review. *Rubber Chem. Technol.* 73, 504–523.
- Caseiro, J.F., Valente, R.A.F., Real, A., Kiendl, J., Auricchio, F., Alves de Sousa, R.J., 2015. Assumed Natural Strain NURBS-based solid-shell element for the analysis of large deformation elasto-plastic thin-shell structures. *Comput. Methods Appl. Mech. Eng.* 284, 861–880.
- Choo, J., Sun, W., 2018. Cracking and damage from crystallization in pores: coupled chemo-hydro-mechanics and phase-field modeling. *Comput. Methods Appl. Mech. Eng.* 335, 347–379.
- Duarte, C.A., Hamzeh, O.N., Liszka, T.J., Tworzydło, W.W., 2001. A generalized finite element method for the simulation of three-dimensional dynamic crack propagation. *Comput. Methods Appl. Mech. Eng.* 190, 2227–2262.
- Francfort, G.A., Marigo, J.J., 1998. Revisiting brittle fracture as an energy minimization problem. *J. Mech. Phys. Solids* 46, 1319–1342.
- Geelen, R.J.M., Liu, Y., Hu, T., Tupek, M.R., Dolbow, J.E., 2019. A phase-field formulation for dynamic cohesive fracture. *Comput. Methods Appl. Mech. Eng.* 348, 680–711.
- Gerasimov, T., De Lorenzis, L., 2016. A line search assisted monolithic approach for phase-field computing of brittle fracture. *Comput. Methods Appl. Mech. Eng.* 312, 276–303.
- Hauptmann, R., Schweizerhof, K., Doll, S., 2000. Extension of the ‘solid-shell’ concept for application to large elastic and large elastoplastic deformations. *Int. J. Numer. Methods Eng.* 49, 1121–1141.
- Heinrich, G., Kaliske, M., 1997. Theoretical and numerical formulation of a molecular based constitutive tube-model of rubber elasticity. *Computat. Theor. Polym. Sci.* 7, 227–241.
- Hocine, N.A., Abdelaziz, M.N., Imad, A., 2002. Fracture problems of rubbers: J-integral estimation based upon eta factors and an investigation on the strain energy density distribution as a local criterion. *Int. J. Fract.* 117, 1–23.
- Li, B., Bouklas, N., 2020. A variational phase-field model for brittle fracture in polydisperse elastomer networks. *Int. J. Solids Struct.* 182, 193–204.
- Li, B., Maurini, C., 2019. Crack kinking in a variational phase-field model of brittle fracture with strongly anisotropic surface energy. *J. Mech. Phys. Solids* 125, 502–522.
- Miehe, C., Göktepe, S., Lulei, F., 2004. A micro-macro approach to rubber-like materials. Part I: the non-affine micro-sphere model of rubber elasticity. *J. Mech. Phys. Solids* 52, 2617–2660.
- Loew, P., Peters, B., Beex, L., 2019. Rate-dependent phase-field damage modeling of rubber and its experimental parameter identification. *J. Mech. Phys. Solids* 127, 266–294.
- Miehe, C., Hofacker, M., Schanzel, L.M., Aldakheel, F., 2015a. Phase field modeling of fracture in multi-physics problems. Part II. Coupled brittle-to-ductile failure criteria and crack propagation in thermo-elastic-plastic solids. *Comput. Methods Appl. Mech. Eng.* 294, 486–522.
- Miehe, C., Hofacker, M., Welschinger, F., 2010. A phase field model for rate-independent crack propagation: Robust algorithmic implementation based on operator splits. *Comput. Methods Appl. Mech. Eng.* 199, 2765–2778.
- Miehe, C., Mauthe, S., Teichtmeister, S., 2015b. Minimization principles for the coupled problem of Darcy-Biot-type fluid transport in porous media linked to phase field modeling of fracture. *J. Mech. Phys. Solids* 82, 186–217.
- Miehe, C., Schanzel, L.-M., 2014. Phase field modeling of fracture in rubbery polymers. Part I: finite elasticity coupled with brittle failure. *J. Mech. Phys. Solids* 65, 93–113.
- Nguyen, T.T., Yvonnet, J., Zhu, Q.Z., Bornert, M., Chateau, C., 2016. A phase-field method for computational modeling of interfacial damage interacting with crack propagation in realistic microstructures obtained by microtomography. *Comput. Methods Appl. Mech. Eng.* 312, 567–595.
- Ogden, R.W., 1997. *Non-Linear Elastic Deformations*. Dover Publications, Mineola, NY.
- Ortiz, M., Pandolfi, A., 1999. Finite-deformation irreversible cohesive elements for three-dimensional crack-propagation analysis. *Int. J. Numer. Methods Eng.* 44, 1267–1282.
- Paggi, M., Reinoso, J., 2017. Revisiting the problem of a crack impinging on an interface: a modeling framework for the interaction between the phase field approach for brittle fracture and the interface cohesive zone model. *Comput. Methods Appl. Mech. Eng.* 321, 145–172.
- Pandolfi, A., Guduru, P.R., Ortiz, M., Rosakis, A.J., 2000. Three dimensional cohesive-element analysis and experiments of dynamic fracture in C300 steel. *Int. J. Solids Struct.* 37, 3733–3760.
- Pandolfi, A., Ortiz, M., 2012. An eigenerosion approach to brittle fracture. *Int. J. Numer. Methods Eng.* 92, 694–714.
- Sabnis, P.A., Forest, S., Cormier, J., 2016. Microdamage modelling of crack initiation and propagation in FCC single crystals under complex loading conditions. *Comput. Methods Appl. Mech. Eng.* 312, 468–491.
- Sargado, J.M., Keilegavlen, E., Berre, L., Nordbotten, J.M., 2018. High-accuracy phase-field models for brittle fracture based on a new family of degradation functions. *J. Mech. Phys. Solids* 111, 458–489.
- Seles, K., Jurcovic, A., Tonkovic, Z., Soric, J., 2019. Crack propagation prediction in heterogeneous microstructure using an efficient phase-field algorithm. *Theor. Appl. Fract. Mech.* 100, 289–297.



- Shanthraj, P., Svendsen, B., Sharma, L., Roters, F., Raabe, D., 2017. Elasto-viscoplastic phase field modelling of anisotropic cleavage fracture. *J. Mech. Phys. Solids* 99, 19–34.
- Shen, R., Waisman, H., Guo, L., 2019. Fracture of viscoelastic solids modeled with a modified phase field method. *Comput. Methods Appl. Mech. Eng.* 346, 862–890.
- Song, J.-H., Wang, H., Belytschko, T., 2008. A comparative study on finite element methods for dynamic fracture. *Comput. Mech.* 42, 239–250.
- Simo, J.C., Armero, F., 1992. Geometrically nonlinear enhanced-strain mixed methods and the method of incompatible modes. *Int. J. Numer. Methods Eng.* 33, 1413–1449.
- Simo, J.C., Rifai, M.S., 1990. A class of mixed assumed strain methods and the method of incompatible modes. *Int. J. Numer. Methods Eng.* 29, 1595–1638.
- Sukumar, N., Moes, N., Moran, B., Belytschko, T., 2000. Extended finite element method for three-dimensional crack modelling. *Int. J. Numer. Methods Eng.* 48, 1549–1570.
- Tang, S., Zhang, G., Guo, T.F., Guo, X., Liu, W.K., 2019. Phase field modeling of fracture in nonlinearly elastic solids via energy decomposition. *Comput. Methods Appl. Mech. Eng.* 347, 477–494.
- Tannéa, E., Li, T., Bourdin, B., Marigo, J.-J., Maurini, C., 2018. Crack nucleation in variational phase-field models of brittle fracture. *J. Mech. Phys. Solids* 110, 80–99.
- Thiagarajan, G., Hsia, K.J., Huang, Y., 2004. Finite element implementation of virtual internal bond model for simulating crack behavior. *Eng. Fract. Mech.* 71, 401–423.
- Videla, J., Natarajan, S., Bordas, S.P.A., 2019. A new locking-free polygonal plate element for thin and thick plates based on Reissner-Mindlin plate theory and assumed shear strain fields. *Comput. Struct.* 220, 32–42.
- Wilson, Z.A., Landis, C.M., 2016. Phase-field modeling of hydraulic fracture. *J. Mech. Phys. Solids* 96, 264–290.
- Wu, J.-Y., Vinh Phu, N., 2018. A length scale insensitive phase-field damage model for brittle fracture. *J. Mech. Phys. Solids* 119, 20–42.
- Wu, J., McAuliffe, C., Waisman, H., Deodatis, G., 2016. Stochastic analysis of polymer composites rupture at large deformations modeled by a phase field method. *Comput. Methods Appl. Mech. Eng.* 312, 596–634.
- Zhang, P., Klein, P., Huang, Y., Gao, H., Wu, P.D., 2002. Numerical simulation of cohesive fracture by the virtual-internal-bond model. *Cmes-Comput. Model. Eng. Sci.* 3, 263–277.